


# Extreme-Mass-Ratio Inspirals Embedded in Dark Matter Halo II: Chaotic Imprints in Gravitational Waves

Surajit Das<sup>1,2</sup><sup>\*</sup>, Surojit Dalui<sup>3</sup><sup>†</sup>, Bum-Hoon Lee<sup>3,4,5</sup><sup>‡</sup> and Yi-Fu Cai<sup>1,2</sup><sup>§</sup>

<sup>1</sup>*Department of Astronomy, School of Physical Sciences,  
University of Science and Technology of China,  
Hefei, Anhui 230026, China*

<sup>2</sup>*CAS Key Laboratory for Researches in Galaxies and Cosmology,  
School of Astronomy and Space Science,  
University of Science and Technology of China,  
Hefei, Anhui 230026, China*

<sup>3</sup>*Department of Physics,  
Shanghai University, 99 Shangda Road,  
Baoshan District, Shanghai 200444, China*

<sup>4</sup>*Center for Quantum Spacetime,  
Sogang University, Seoul 04107, Korea*

<sup>5</sup>*Department of Physics,  
Sogang University, Seoul 04107, Korea*

We investigate the imprints of chaos in gravitational waves from extreme-mass-ratio inspirals configuration, where a stellar massive object, confined in a harmonic potential, orbits a supermassive Schwarzschild-like black hole embedded in a Dehnen-type dark matter halo. In our first paper [1], we demonstrated the system's transition from non-chaotic to chaotic dynamics by analyzing Poincaré sections, orbital evolution, and Lyapunov exponents across different energies and dark matter halo parameters. In this work, we compute the gravitational waveforms of the small celestial object along different chaotic and non-chaotic orbits by implementing the numerical kludge scheme. We further perform a spectral analysis of the gravitational waveforms from such orbits. In particular, we show that when the system is in a chaotic state, the gravitational wave signals are characterized by broader frequency spectra with finite widths, enhanced amplitude and energy emission rate, distinctly differentiating them from the signals generated during the system's non-chaotic state. Through recurrence analysis we also show that the time series of gravitational waveforms strain carry unique information on the motion of chaotic dynamics, which can be used to distinctly differentiate from non-chaotic to chaotic motion of the source. Furthermore, we discuss the potential detectability of these orbits for upcoming observatories like LISA, TianQin, and Taiji, emphasizing the significant potential for detecting chaotic imprints in gravitational waves to substantially enhance our understanding of chaotic dynamics in black hole physics and the dark matter environments of galactic nuclei.

## I. INTRODUCTION

The groundbreaking detection of gravitational waves (GWs) by the LIGO and Virgo scientific teams represented a pivotal moment in the fields of gravitational wave astronomy [2–8]. This discovery initiated a brand new epoch in astronomical observation. For example, astrophysical systems such as double white dwarfs [9, 10], massive binary black holes [11, 12], stellar-mass binary black holes [13, 14], and extreme-mass-ratio inspirals

(EMRIs) [15, 16] are predicted to emit GW signals predominantly in the millihertz (mHz) frequency band. Investigating these phenomena is crucial for deepening our understanding of gravitational physics and the astrophysical processes underlying GWs sources.

Space-based GWs detectors are specifically designed to explore the mHz frequency domain [17–19]. Among anticipated sources, EMRIs are particularly significant, which typically the inspirals of stellar-mass compact objects (of mass approximately  $10^0 M_\odot - 10^1 M_\odot$ ) around a supermassive black hole (SMBH) (of mass approximately  $10^5 M_\odot - 10^{10} M_\odot$ ), frequently found in galactic nuclei. The prolonged duration of EMRIs signals that lasts thousands to millions of cycles offers a unique opportunity to perform precision tests of general relativity in the strong-field regime [20–24]. With the high sensitivity and long observation baseline of these future space missions, it will be possible to detect subtle dynamical effects encoded in

---

<sup>\*</sup> [surajitdas@mail.ustc.edu.cn](mailto:surajitdas@mail.ustc.edu.cn), [surajit.cbpbu20@gmail.com](mailto:surajit.cbpbu20@gmail.com); (corresponding author)

<sup>†</sup> [surojitdalui@shu.edu.cn](mailto:surojitdalui@shu.edu.cn); (corresponding author)

<sup>‡</sup> [bhl@sogang.ac.kr](mailto:bhl@sogang.ac.kr); (corresponding author)

<sup>§</sup> [yifucai@ustc.edu.cn](mailto:yifucai@ustc.edu.cn); (corresponding author)

the waveforms, thereby enhancing our understanding of gravity in the strong-field regime.

Despite this great scientific potential, significant challenges persist in developing accurate theoretical waveform templates for EMRI systems from observational data. Many theoretical and computational approaches have been attempted. In this work, we particularly focus on gravitational waves emitted by EMRI system from the perspective of chaotic dynamics. The following is the motivational factor. Since chaos denotes the sensitivity and unpredictability of an object's motion, it is expected to explain many significant nonlinear events of a binary system of interest in general relativity and beyond. Since the sensitivity of an object's motion can be determined by chaos, it is reasonable to think about how much significant information we can obtain from studying chaos. Chaos in gravity has attracted a lot of attention lately, numerous studies have been conducted on this subject [25–45]. Classically, substantial efforts have been devoted to understanding how the presence of horizon of black holes (BHs) can make an integrable system transit from regular to chaotic motion. Such studies cover diverse scenarios, including spinning BHs [33–35], magnetized BHs [38], and involve test particle with varying mass, charge [39], spin [30, 33, 34], massive particle [36], massless particle [42] and as well as in modified gravity [45]. Additionally, chaos has been investigated in realistic astrophysical binary systems as well [46–50].

In a real astrophysical scenario, BHs rarely exist in isolation, instead, they inhabit dynamically rich and complex environments. For instance, SMBHs are known as driving forces of active galactic nuclei [51, 52]. Astrophysical and cosmological observations strongly suggest that most galaxies, including our Milky Way, are embedded in massive DM halos [53–57]. Therefore investigating gravitational interactions between DM halos and SMBHs is essential for understanding the role of DM in galactic-scale structures. Studying various DM models thereby helps address persistent theoretical challenges in gravitational physics and enriches our grasp of fundamental physics. Numerous astrophysically relevant DM halo models have been explored extensively in Refs. [58–69] and offering insights into BHs, which are embedded in DM halos (see [70, 71] and references therein).

Recent research has focused significantly on the impact of Dehnen-type DM halos [72] on BH dynamics and structures, exploring consequences for star cluster survivability [66, 73], ultra-faint dwarf galaxy evolution [74] and thermodynamics in composite BH-DM system [75]. Such environments naturally raise the question of how these complex surroundings modify the onset and character of chaotic dynamics because the presence of DM compositions greatly influence the horizon structure. According to current research, realistic DM halos can significantly change near-horizon dynamics, which could improve chaotic aspects in EMRI systems. Additionally, it is anticipated that chaos will leave distinct marks on gravitational wave signals, such as distorted phase co-

herence, expanded spectrum characteristics, or broader amplitude modulations. These could serve as observational markers of strong-field nonlinear dynamics and as probes of galactic environments near SMBHs.

In the first work of our series [1], we investigated the chaotic dynamical phenomena in EMRI-like configuration, where a stellar-mass compact object orbiting close to the horizon of a supermassive Schwarzschild BH embedded in a Dehnen-(1, 4, 5/2) type DM halo. Therefore one can model the dynamics of the secondary inspiral as the motion of a relativistic massive particle on the background of the primary BH-DM halo combined spacetime. Our focus was on understanding the dynamical behavior of the massive particle close to the horizon in the background of such BH-DM halo combined spacetime and how the horizon influences if the particle is a part of an integrable system, and that integrable system perturbs the combined BH-DM halo background. To investigate the horizon's influence, we analyzed the dynamics of a relativistic massive particle that is subject to external potentials and is moving around a BH embedded in a DM halo environment. As a consequence, this allowed us to explore bounded motion near the BH horizon and identify how small perturbations evolve under the combined influence of BH and the surrounding DM field. Finally, we analyzed the phase-space dynamics through Poincaré sections, quantify sensitivity to initial conditions using Lyapunov exponents, and discuss how chaos emerges as a function of the halo parameters.

In this work as the second part of our series started with [1], we use the numerical kludge method in order to generate the gravitational waveforms emitted by such EMRI configuration as discussed in [1] and then particularly focus on the point that how chaos affects gravitational waves. We systematically compare the generated waveforms, the frequency and energy spectra of the gravitational waves from those non-chaotic, onset-of-chaotic and chaotic orbits, which are influenced by the DM halo parameters and then analyze the imprints of chaos in gravitational waves. We discuss the clear difference of gravitational waves between a non-chaotic and a chaotic EMRIs in the background of our considered BH-DM halo combined system. Moreover, to establish the influence of DM halo parameters on chaotic dynamics and its features on the resulting gravitational waveforms, we further study the recurrence analysis and phase space reconstruction for both, the radial motion as well as the gravitational strains. One of the novel findings we obtain in this case is the possible detection of chaos through gravitational waves via characteristic strain sensitivity, and that could be detectable by the future space-based detectors, which provides a new insight into BH astrophysics and the influence of galactic settings on the dynamics of compact objects.

The paper is organized as follows. In Sec. II, we discuss in brief on the chaotic dynamics of EMRI configuration in the background of a Schwarzschild-like BH solution immersed within a Dehnen(1, 4, 5/2)-type DM halo. In

Sec. III, we employ a numerical kludge scheme to generate gravitational waveforms, analyzing their characteristic patterns, averaged amplitude and energy emission rate, frequency spectra and energy spectra. Sec. IV demonstrates the signatures of chaos in gravitational waveforms through recurrence analysis. Finally in Sec. V, we assess the detectability of chaotic gravitational wave signals by future space-based gravitational wave detectors, including LISA, TianQin, and Taiji. We conclude the findings of our study in Sec. VI.

## II. CHAOTIC DYNAMICS OF EXTREME-MASS-RATIO INSPIRALS AROUND A SCHWARZSCHILD BLACK HOLE-DARK MATTER HALO

We start by considering a static spherically symmetric (SSS) BH configuration embedded within galaxies that are surrounded by a Dehnen type DM halo profile [72, 76]. Considering a SSS spacetime ansatz in a Dehnen type DM halo as

$$ds^2 = -f(r)dt^2 + \frac{dr^2}{f(r)} + r^2 d\Omega^2, \quad (1)$$

with  $d\Omega^2 = d\theta^2 + \sin^2\theta d\phi^2$  representing the line element on a unit two-sphere. The double power-law density distributions of DM halos and elliptical galaxies is given by [72, 76]

$$\rho = \rho_s \left(\frac{r}{r_s}\right)^{-\gamma} \left[ \left(\frac{r}{r_s}\right)^\alpha + 1 \right]^{\frac{\gamma-\beta}{\alpha}}, \quad (2)$$

where  $\alpha, \beta, \gamma$  are free parameters and  $\rho_s, r_s$  are known as the typical density and scale radius of the central DM halo, respectively. Here we consider a SSS BH solution in galaxies surrounded by a Dehnen- $(\alpha, \beta, \gamma) \equiv (1, 4, 5/2)$  type DM halo, whose BH solution for  $f(r)$  up to leading order is given by [77]

$$f(r) = 1 - \frac{2M}{r} - 32\pi\rho_s r_s^2 \sqrt{1 + \frac{r_s}{r}}, \quad (3)$$

where  $M$  is the mass of the BH. In the current study, we will conduct our entire analysis using this specific galactic Schwarzschild-like BH solution (Eq. (3)). For more details on the solution of Schwarzschild-like BH embedded in a Dehnen- $(1, 4, 5/2)$  type DM halo, see [77] and the references therein.

Now we review the dynamics of a massive probe particle in a BH-DM halo combined spacetime. We are specifically interested in examining how the DM halo parameters  $(\rho_s, r_s)$  influence a massive test particle situated near the event horizon of a Schwarzschild-like BH embedded in a galactic DM halo. To facilitate this investigation, we adopt a more suitable coordinate system, the Painlevé-Gullstrand (PG) coordinates [78], within the SSS BH-DM halo spacetime (Eq. (1)). Under the

Painlevé-Gullstrand transformation, Eq. (1) transforms to a non-singular metric at the horizon, as the following.

$$ds^2 = -f(r)dt^2 + 2\sqrt{1-f(r)}dt dr + dr^2 + r^2 d\Omega^2. \quad (4)$$

To derive the equations of motion for a massive test particle orbiting in the background spacetime of combined BH and DM halo (Eq. (4)), one can start with the Lagrangian of a massive test particle of mass  $m$ , subject to an external potential, which is given by [1],

$$\mathcal{L} = -m\sqrt{f(r) - 2\sqrt{1-f(r)}\dot{r} - \dot{r}^2 - r^2\dot{\phi}^2} - (a(r) + b(\phi)). \quad (5)$$

In the above expression, the equatorial plane symmetry is considered (i.e.,  $\theta = \pi/2$ ) and  $a(r), b(\phi)$  are two external potentials acting in the radial and angular directions, respectively.

From the preceding Lagrangian, the generalized momenta corresponding to the  $r$  and  $\phi$  coordinates are given by:

$$p_r = \frac{m(\dot{r} + \sqrt{1-f(r)})}{\sqrt{f(r) - 2\sqrt{1-f(r)}\dot{r} - \dot{r}^2 - r^2\dot{\phi}^2}},$$

$$p_\phi = \frac{mr^2\dot{\phi}}{\sqrt{f(r) - 2\sqrt{1-f(r)}\dot{r} - \dot{r}^2 - r^2\dot{\phi}^2}}. \quad (6)$$

Therefore the conserved energy for the massive test particle can be written as:

$$E = p_r \dot{r} + p_\phi \dot{\phi} - \mathcal{L}$$

$$= -\sqrt{1-f(r)}p_r \pm \sqrt{p_r^2 + \frac{p_\phi^2}{r^2} + m^2} + (a(r) + b(\phi)), \quad (7)$$

Given our focus on dynamics extremely close to the horizon, our analysis specifically concerns outgoing particle (i.e., considering the positive sign only). Accordingly, one can derive the following set of dynamical equations of motion:

$$\frac{dr}{dt} = \frac{\partial E}{\partial p_r} = -\sqrt{1-f(r)} + \frac{p_r}{\sqrt{p_r^2 + \frac{p_\phi^2}{r^2} + m^2}}, \quad (8)$$

$$\frac{dp_r}{dt} = -\frac{\partial E}{\partial r} = -\frac{\partial_r f(r)}{2\sqrt{1-f(r)}}p_r + \frac{p_\phi^2/r^3}{\sqrt{p_r^2 + \frac{p_\phi^2}{r^2} + m^2}} - \partial_r a(r), \quad (9)$$

$$\frac{d\phi}{dt} = \frac{\partial E}{\partial p_\phi} = \frac{p_\phi/r^2}{\sqrt{p_r^2 + \frac{p_\phi^2}{r^2} + m^2}}, \quad (10)$$

$$\frac{dp_\phi}{dt} = -\frac{\partial E}{\partial \phi} = -\partial_\phi b(\phi). \quad (11)$$

The equations above form the basis for the numerical investigations on chaotic dynamics. The rationale for

employing the Painlevé-Gullstrand coordinate transformation, together with the specification of the Lagrangian for a massive probe particle that is influenced by an external potentials, is provided in our earlier work [1], where a comprehensive treatment of these topics can be found.

Now we review the chaotic dynamics of EMRIs (where the mass ratio is taken to be  $m/M = 10^{-5}$ ), which involve a stellar-mass compact object in orbit around a supermassive Schwarzschild-like BH, enveloped by a Dehnen(1, 4, 5/2)-type DM halo in galaxies. In our earlier work [1], we systematically examined the transitions from a non-chaotic (regular or periodic) to chaotic dynamical behavior of a massive test particle close to the horizon under an EMRI configuration by analyzing the nonlinear dynamical systems of equations given by Eqs. (8), (9), (10), and (11). This investigation has carried out by properly investigating the associated Poincaré sections, EMRI orbital evolutions, and both total, radial Lyapunov exponents as functions of energy and DM halo parameters  $\rho_s$  and  $r_s$ . This sequence of analyses elucidates the influence of both the event horizon of the galactic Schwarzschild-like BH embedded in the DM halo and the particular parameters of the halo ( $\rho_s$ ,  $r_s$ ) on the emergence of chaotic motion for a massive test particle. In the current paper, we primarily concentrate on the GWs consequences arising from such chaotic orbital EMRIs, and therefore we summarize the key findings from our previous study [1] in the following Table I.

### III. NUMERICAL KLUDGE GRAVITATIONAL WAVEFORMS FROM EMRI

In the analysis of BH binary system in our study, it is usual to model the supermassive BH-DM halo combined system—as the primary body, while a less massive stellar compact object is treated as a secondary test particle. Hence a stellar massive compact object moving in a chaotic and non-chaotic orbits around a supermassive BH surrounded by a DM halo in galaxies constitutes an EMRIs system. As the secondary approaches close to the primary, the strong gravitational field alters spacetime curvature, producing GWs. These waves extract energy and angular momentum from the test particle, causing it to gradually spiral inward. Over short timescales, the energy and angular momentum lost due to the secondary’s motion are insignificant relative to the system’s total energy, justifying the use of the adiabatic approximation [79–83]. This approximation posits that energy and angular momentum remain approximately constant over an orbital period, allowing any back reactions (such as gravitational radiation effects on the test particle’s motion and the DM halo) to be neglected. Consequently, the secondary’s motion can be described using geodesic equations, and the resulting gravitational waveforms can be approximated via the quadrupole formula using the “Kludge” method [84–86]. Therefore, the gravitational waves produced by the EMRIs contain

information about both chaotic and non-chaotic orbits, as well as the influence of the DM halo parameters  $\rho_s$  and  $r_s$  (which we have analyzed in our first work [1] in Sec. IV), that how DM halo parameters play a significant role in chaotic and non-chaotic dynamics of a secondary test particle.

When a small massive object follows a non-chaotic orbit around a supermassive BH surrounded by a DM halo, it traces a closely overlapping trajectories (as illustrated in the first column of Fig. 11 of our previous paper [1]). In contrast, for chaotic orbits, variations in energy and DM halo parameters cause the particle to make them random, reducing the overlap between two initially close trajectories (see the third columns of Fig. 11 in our paper [1]) and therefore, near the event horizon, chaotic orbit undergoes prolonged, high-frequency oscillations, producing more rich GW signals. These waves encode essential information about the physics near the BH’s event horizon, making them an effective tool for investigating BH properties incorporated with DM halos through both chaotic and non-chaotic orbital dynamics. Thus, the GWs generated by EMRIs establish a direct connection between two different kind of motions (chaotic and non-chaotic in our case) of the secondary and the fundamental properties of the BH-DM halo combined spacetime. This provides an opportunity to investigate both the behavior of compact objects and the essential features of BHs in the immediate vicinity of the event horizon within our galaxy.

The numerical kludge waveform approach involves combining a fully relativistic particle’s motion with an approximate model for GWs emission [86]. To implement such method in our case, we first obtain the secondary’s trajectory, which is generated in “phase space” defined in the equatorial plane with constant energy and angular momentum in PG coordinates, as discussed in Sec. II. Next, the dynamics of a secondary object around Schwarzschild BH-DM halo spacetime are numerically integrated along the orbiting secondary’s trajectory to compute the coordinates of the object as a function of time.<sup>1</sup> Finally, the kludge gravitational waveform is produced by constructing an “equivalent” trajectory in flat space. This is achieved by projecting the PG coordinates

---

<sup>1</sup> Since we are investigating chaos in the dynamics of a massive test particle and chaotic phenomena is probed by the near-horizon effect, we adopt the PG coordinates due to its regularity across the horizon (see text in Sec. IV of our previous paper [1] for details), avoiding the coordinate singularities present in Schwarzschild coordinates. While GWs emission is typically analyzed in the asymptotic wave zone, where both converge to the same Minkowski limit, the choice of PG coordinates remains physically consistent. This approach ensures precise representation of the chaotic behavior close to the horizon, considering numerical complexity, while remaining consistent with conventional wave extraction techniques in the distant field region.



TABLE I: A principal investigation is shown in the transition from “Non-chaotic (NC)” to “Chaotic (C)” dynamics, passing through the “Onset-of-chaos (OC)” phase, within an EMRI limit, where a stellar-mass compact object inspiraling around a supermassive Schwarzschild-like BH, which is surrounded by a Dehnen-(1, 4, 5/2) type DM halo. The study demonstrates the influence of the energy and the dark matter halo parameters, namely  $\rho_s$  and  $r_s$ , on the orbital dynamics of the EMRI within its galactic environment. For a comprehensive understanding of the findings summarized here, the reader is directed to our preceding work in this series (refer to Figures 8–13 and Table 3 in [1]).

Case description (fixed parameters)	Non-chaotic	Onset-of-chaotic	Chaotic
<b>Case-I:</b> $r_s = 0.15, \rho_s = 0.02$	$E = 108$	$E = 130$	$E = 132.50$
<b>Case-II:</b> $\rho_s = 0.01, r_s = 0.25$	$E = 95$	$E = 118$	$E = 122$
<b>Case-III:</b> $r_s = 0.15, E = 90$	$\rho_s = 0.01$	$\rho_s = 0.04$	$\rho_s = 0.05$
<b>Case-IV:</b> $\rho_s = 0.01, E = 115$	$r_s = 0.10$	$r_s = 0.25$	$r_s = 0.27$
<b>Einstein’s GR:</b> $\rho_s = 0, r_s = 0$	$E = 140$	$E = 154$	$E = 156$

onto a spherical polar coordinate grid. Subsequently, the corresponding coordinate system is defined, as the Cartesian coordinates in flat space, as described below:

$$\begin{aligned} x(t) &= r(t) \sin \theta(t) \cos \phi(t) , \\ y(t) &= r(t) \sin \theta(t) \sin \phi(t) , \\ z(t) &= r(t) \cos \theta(t) . \end{aligned} \quad (12)$$

Before proceeding further, it is important to note that as discussed by Babak *et al.* in their Ref. [86], the use of a derived flat-space trajectory serves solely as an input for the phenomenological waveform-generation modeling. Employing such an approximation results in GW amplitudes that lack precision; however, the derived GW frequencies remain accurate. This specific kludge approach has demonstrated strong performance, achieving approximately 95% accuracy when benchmarked against Teukolsky-based waveforms for EMRIs [86]. Consequently, after determining the trajectory of a secondary particle within a flat spacetime geometry—where the particle orbits a supermassive BH situated within a Dehnen(1, 4, 5/2) DM halo—it becomes feasible to utilize these kludge waveforms. Their acceptable quality enables them to serve a function in the analysis of spaceborne gravitational-wave data, particularly in the search for EMRIs where the central BH is influenced by a galactic DM halo.

In the weak-field regime, expressing the spacetime metric as  $g_{\mu\nu} = \eta_{\mu\nu} + h_{\mu\nu}$ , where  $\eta_{\mu\nu}$  represents the Minkowski metric and  $h_{\mu\nu}$  denotes small metric perturbations (i.e.,  $|h_{\mu\nu}| \ll 1$ ). The trace-reversed metric perturbation is defined through the relation  $\bar{h}^{\mu\nu} \equiv h^{\mu\nu} - \frac{1}{2}\eta^{\mu\nu}h$ , with  $h = \eta^{\mu\nu}h_{\mu\nu}$  being the trace of the perturbation. By imposing the Lorentz gauge condition  $\partial_\alpha \bar{h}^{\mu\alpha} = 0$ , we obtain the linearized Einstein field equations in the form:

$$\square \bar{h}^{\mu\nu} = -16\pi \mathcal{T}^{\mu\nu} , \quad (13)$$

where  $\square$  represents the standard flat-space d’Alembertian operator, and  $\mathcal{T}^{\mu\nu}$  is the effective

energy momentum tensor, obeys the conservation relation  $\partial_\nu \mathcal{T}^{\mu\nu} = 0$ . For gravitational wave detection at large distances, we specifically require the transverse-traceless components of  $\bar{h}^{jk}$ , necessitating an appropriate projection operation. In our coordinate system centered on the supermassive BH with DM halo, designate  $(t, \mathbf{x})$  as the observer’s position and  $(t_p, \mathbf{x}_p)$  as the particle’s position. The solution to the wave equation Eq.(13) takes the familiar retarded potential form as

$$\bar{h}^{ij}(t, \mathbf{x}) = 4 \int \frac{\mathcal{T}^{ij}(t - |\mathbf{x} - \mathbf{x}'|, \mathbf{x}')}{|\mathbf{x} - \mathbf{x}'|} d^3x' . \quad (14)$$

Building upon Ref. [87], Press developed an expression valid for fast motion, extended sources by systematically applying the conservation relation ( $\partial_\nu \mathcal{T}^{\mu\nu} = 0$ ) to Eq. (14). However in the slow-motion approximation, Eq. (14) reduces to the standard quadrupole formula

$$\bar{h}^{ij}(t, \mathbf{x}) = \frac{2}{r} \left[ \ddot{I}^{ij}(t') \right]_{t'=t-r} , \quad (15)$$

where overdots denote time derivatives. The source symmetric and traceless mass quadrupole moment, appearing in the above expression is defined as

$$I^{ij} = \int x^i x^j T^{00} d^3x . \quad (16)$$

Here  $T^{00}$  is the  $tt$ -component of the energy-momentum tensor for the small secondary of  $m$  with trajectory  $Z^i(t)$ , defined as [88]

$$T^{00}(t, x^i) = m \delta^3(x^i - Z^i(t)) . \quad (17)$$

One can also include the next order terms (the mass octupole and current quadrupole moments of the source) in the Press formula. However, the presence of delta-function in the above expression of energy-momentum tensor simplifies the evaluation of the source quadrupole

moment and under the slow-motion limit, we obtain the symmetric and traceless GW source quadrupole formula as [86, 88, 89]

$$h_{ij} = \frac{2}{D_L} \ddot{I}_{ij} = \frac{2m}{D_L} (a_i x_j + a_j x_i + 2v_i v_j), \quad (18)$$

Where  $D_L$  is the luminosity distance to the detector,  $v_i$  and  $a_i$  are spatial velocity and acceleration of the secondary stellar-massive compact object, respectively. Our analysis will focus on the formulations given by Eq. (18). Finally, to analyze the GWs signal at a detector level, we establish a detector-aligned coordinate system  $(X, Y, Z)$  sharing its origin with the original  $(x, y, z)$  frame, both centered on the supermassive BH [89]. The basis vectors of this detector frame in the original coordinates are defined as

$$\mathbf{e}_X = [\cos \zeta, -\sin \zeta, 0], \quad (19)$$

$$\mathbf{e}_Y = [\sin \iota \sin \zeta, -\cos \iota \cos \zeta, -\sin \iota], \quad (20)$$

$$\mathbf{e}_Z = [\sin \iota \sin \zeta, -\sin \iota \cos \zeta, \cos \iota], \quad (21)$$

where  $\zeta$  denotes the pericenter longitude within the orbital plane while  $\iota$  represents the inclination angle between the orbital plane and the  $X - Y$  plane. The GW polarizations can then be derived by projecting the metric perturbations (Eq. (18)) onto the detector frame, as the following:

$$h_+ = \frac{1}{2} (\mathbf{e}_X^i \mathbf{e}_X^j - \mathbf{e}_Y^i \mathbf{e}_Y^j) h_{ij}, \quad (22)$$

$$h_\times = \frac{1}{2} (\mathbf{e}_X^i \mathbf{e}_Y^j + \mathbf{e}_Y^i \mathbf{e}_X^j) h_{ij}. \quad (23)$$

Hence using Eqs. (19), (20) and Eqs. (22), (23) the polarizations can be described using the components  $h_{\zeta\zeta}$ ,  $h_{\iota\iota}$ , and  $h_{\iota\zeta}$ , which are formulated in the detector frame as specific combinations of the  $h_{ij}$  elements:

$$h_+ = (h_{\zeta\zeta} - h_{\iota\iota})/2, \quad (24)$$

$$h_\times = h_{\iota\zeta}, \quad (25)$$

where the components  $h_{\zeta\zeta}$ ,  $h_{\iota\iota}$ , and  $h_{\iota\zeta}$  are expressed as the following forms [86, 90].

$$h_{\zeta\zeta} = h_{xx} \cos^2 \zeta - h_{xy} \sin 2\zeta + h_{yy} \sin^2 \zeta, \quad (26)$$

$$h_{\iota\iota} = \cos^2 \iota [h_{xx} \sin^2 \zeta + h_{xy} \sin 2\zeta + h_{yy} \cos^2 \zeta] \\ + h_{zz} \sin^2 \iota - \sin 2\iota [h_{xz} \sin \zeta + h_{yz} \cos \zeta], \quad (27)$$

$$h_{\iota\zeta} = \cos \iota \left[ \frac{1}{2} h_{xx} \sin 2\zeta + h_{xy} \cos 2\zeta - \frac{1}{2} h_{yy} \sin 2\zeta \right] \\ + \sin \iota [h_{yz} \sin \zeta - h_{xz} \cos \zeta]. \quad (28)$$

This approach, while approximate and applicable only for the secondary body's small orbital velocities, leads to an adiabatic progression of EMRIs. In the subsequent sections that follow, we conduct a comprehensive investigation of GWs utilizing the methodology outlined in this section.

## A. Analysis of the generated gravitational waveforms

To investigate how the central density  $\rho_s$  and scale radius  $r_s$  of the DM halo affect the GWs emission, we study a secondary stellar-massive compact object of mass  $m = 10 M_\odot$  orbiting a supermassive Schwarzschild-like BH embedded in a Dehnen(1, 4, 5/2) type DM halo with mass  $M = 10^6 M_\odot$ . The system is assumed to be at a luminosity distance of  $D_L = 2 \text{ Gpc}$ . This setup allows us to analyze GWs generated by both chaotic and non-chaotic orbital trajectories under the influence of a Dehnen(1, 4, 5/2)-type DM halo. For simplicity, we set the inclination angle  $\iota = \pi/4$  and pericenter longitude  $\zeta = \pi/4$  to calculate the polarizations of GWs.

Fig. 1 shows the gravitational waveforms from an EMRI system, where a secondary object orbits a supermassive Schwarzschild-like BH embedded in a Dehnen(1, 4, 5/2)-type DM halo. The waveforms have the hidden gravitational influences of the Dehnen(1, 4, 5/2)-type DM halo on the formation of the respective chaotic and non-chaotic orbits. Additionally, we have also generated the waveforms for the onset-of-chaos orbits (i.e., the first appearance of the broken tori in the associated Poincaré sections), situated between non-chaotic and chaotic orbits, to illustrate the transition from orderly motion to irregular or chaotic dynamics (see our first work [1] for further clarification).

Fig. 1 also shows that the overall amplitudes remain nearly constant for non-chaotic orbits (as one can visualize the waveforms from non-chaotic orbits in the insets of each four figures). However, as chaos begins to influence the dynamics (evident from the first appearance of broken tori in the associated Poincaré sections as the ‘‘onset-of-chaos’’), the amplitudes of each polarization mode start fluctuating. Eventually, for chaotic orbits, they exhibit irregular and non-constant behavior.

To understand it more clearly, we have also presented an enlarged view of the gravitational waveforms emitted by such EMRI system for non-chaotic, onset-of-chaos, and chaotic orbits, focusing on two different cases: The Case-III is on varying the central density parameter  $\rho_s$  with fixed energy  $E = 90$  and scale radius  $r_s = 0.15$  (see Fig. 2). The Case-IV, which is on varying the scale radius  $r_s$  with fixed energy  $E = 115$  and central density  $\rho_s = 0.01$  (see Fig. 3). The waveforms associated with the non-chaotic orbits exhibit an overall periodic patterns, despite variations in the amplitude of individual modes (Figs. 2(a), 2(d) for  $\rho_s = 0.01$  and Figs. 3(a), 3(d) for  $r_s = 0.10$ , respectively). This behavior is consistent with the Poincaré sections for this non-chaotic orbit, as discussed in the first part of this series [1]. In contrast, as chaos begins to influence the dynamics, the periodicity observed in Figs. 2(b), 2(e) for  $\rho_s = 0.04$  and Figs. 3(b), 3(e) for  $r_s = 0.25$  start to degrade. Finally, in the chaotic regime (for  $\rho_s = 0.05$  and  $r_s = 0.27$ ), the waveforms lose their periodic structure entirely, displaying irregular fluctuating pattern. These findings are in agreement with

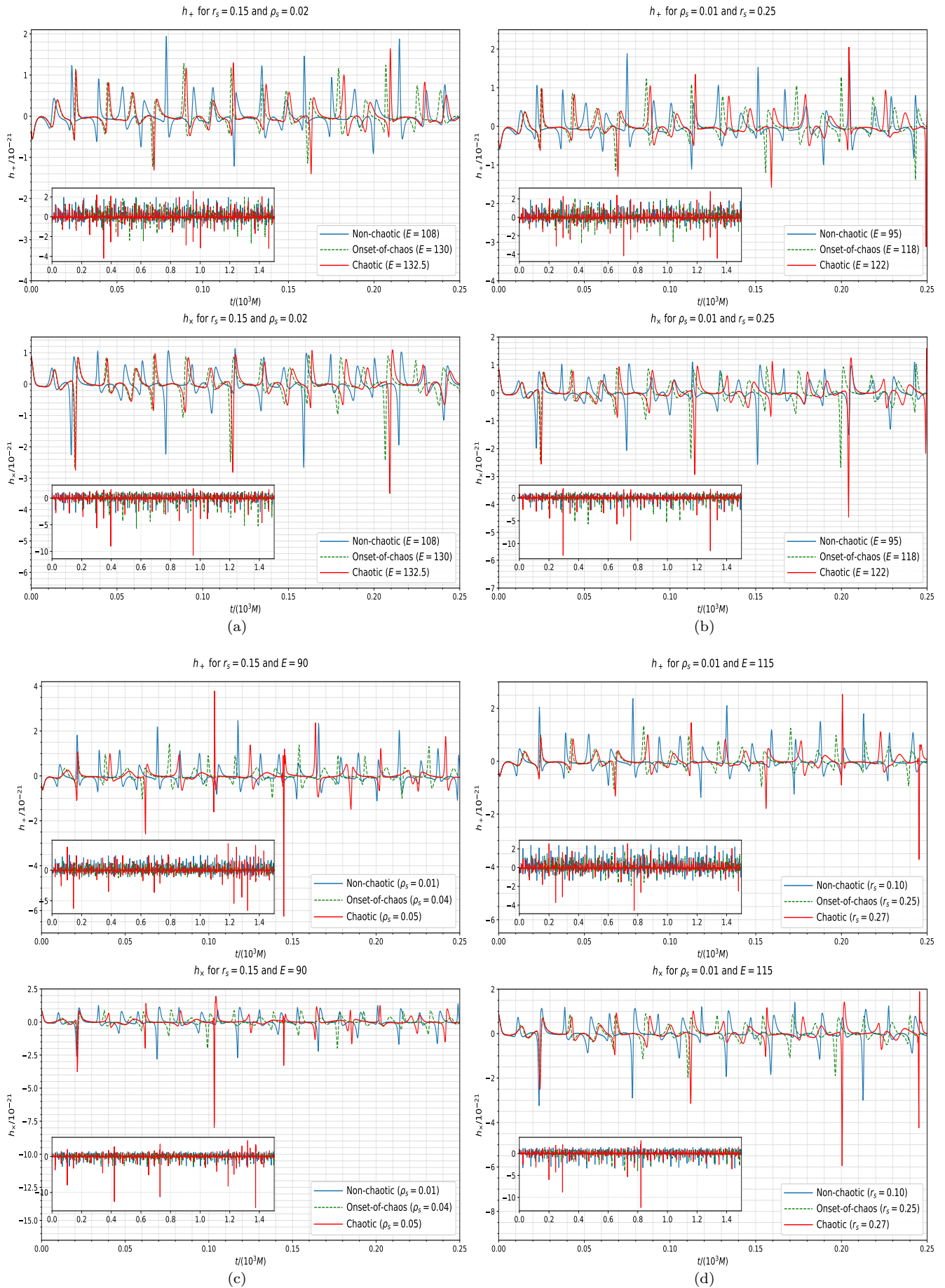


FIG. 1: The gravitational waveforms of the + and  $\times$  modes corresponding to the non-chaotic, onset-of-chaos and chaotic orbits for the four different cases (Table I). The time range is taken from 0 to 0.25 in unit of  $t/(10^3M)$ , whereas the rectangular box inserted in each figure display of an extended view of the corresponding waveforms over an extended time range (from 0 to 1.5 in unit of  $t/(10^3M)$ ).

the Poincaré maps analyzed in our work [1] and reveals how different DM halo parameters affect on the formation of chaotic dynamics in such EMRIs, considered in our text.

Next, we would like to briefly discuss on how chaotic and non-chaotic orbit evolve over time by studying the averaged amplitude and energy emission rate of their respective GWs. As stated by the quadrupole formula under kludge scheme, the averaged gravitational wave am-

plitude across all directions can be expressed as [91]

$$A \propto \sqrt{\ddot{I}_{ij}\ddot{I}^{ij}}, \quad (29)$$

and the power radiated by the GWs can be described as [91]

$$\frac{d\mathcal{E}}{dt} = -\frac{\ddot{I}_{ij}^2}{45}. \quad (30)$$

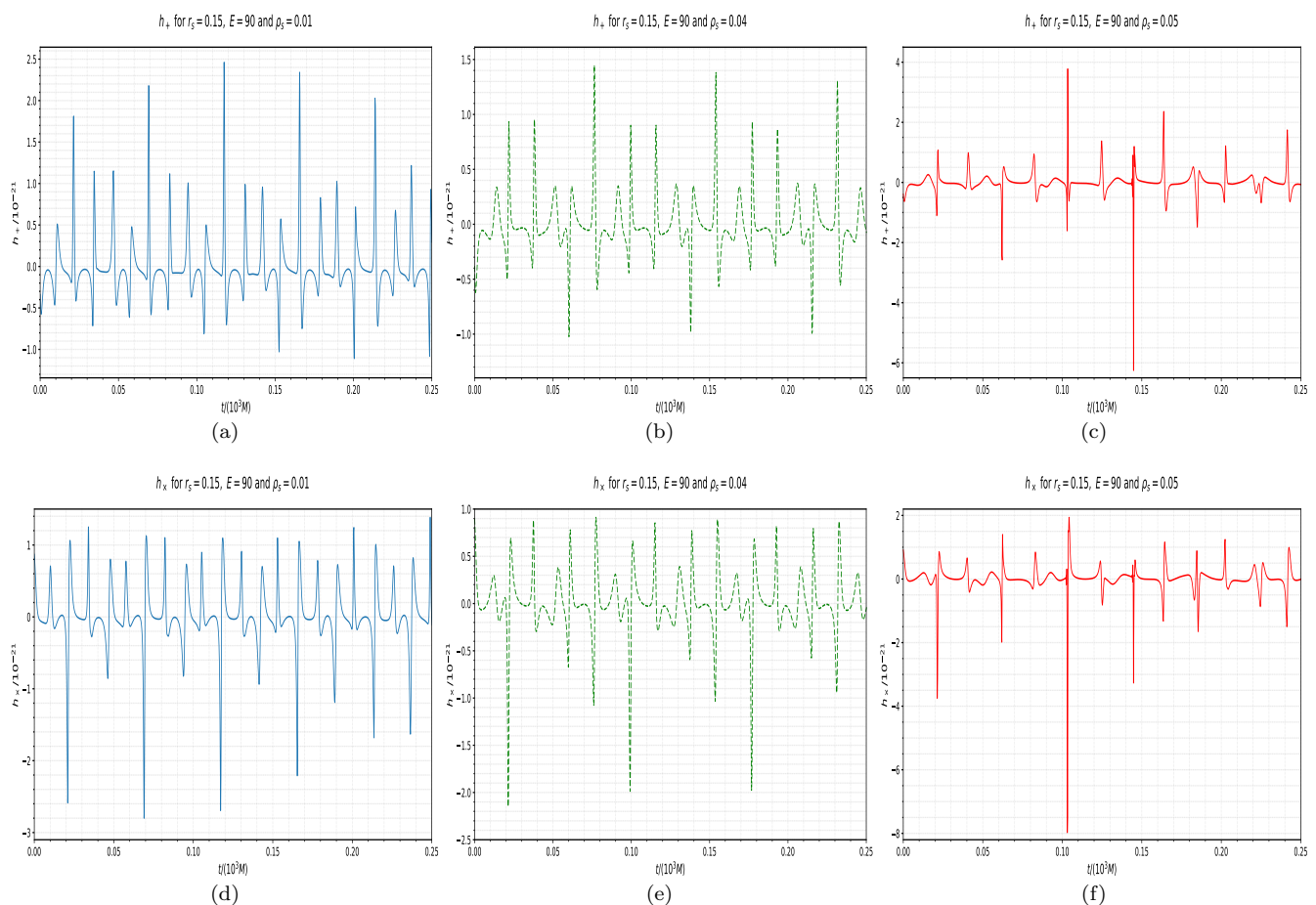


FIG. 2: Gravitational waveforms of the + and  $\times$  modes corresponding to the non-chaotic, onset-of-chaos and chaotic orbits for fixed  $r_s = 0.15$ ,  $E = 90$  with variations in density parameter  $\rho_s$  as our considered Case-III. Here the time range is shown from 0 to 0.25 in unit of  $t/(10^3M)$ .



Here the negative sign in the above expression implies for the loss of energy by radiation. It is important to emphasize that the amount (numerical value) of energy lost is extremely small, so that its impact on dynamical mo-

tion remains entirely negligible, even for celestial objects observed over long timescales.

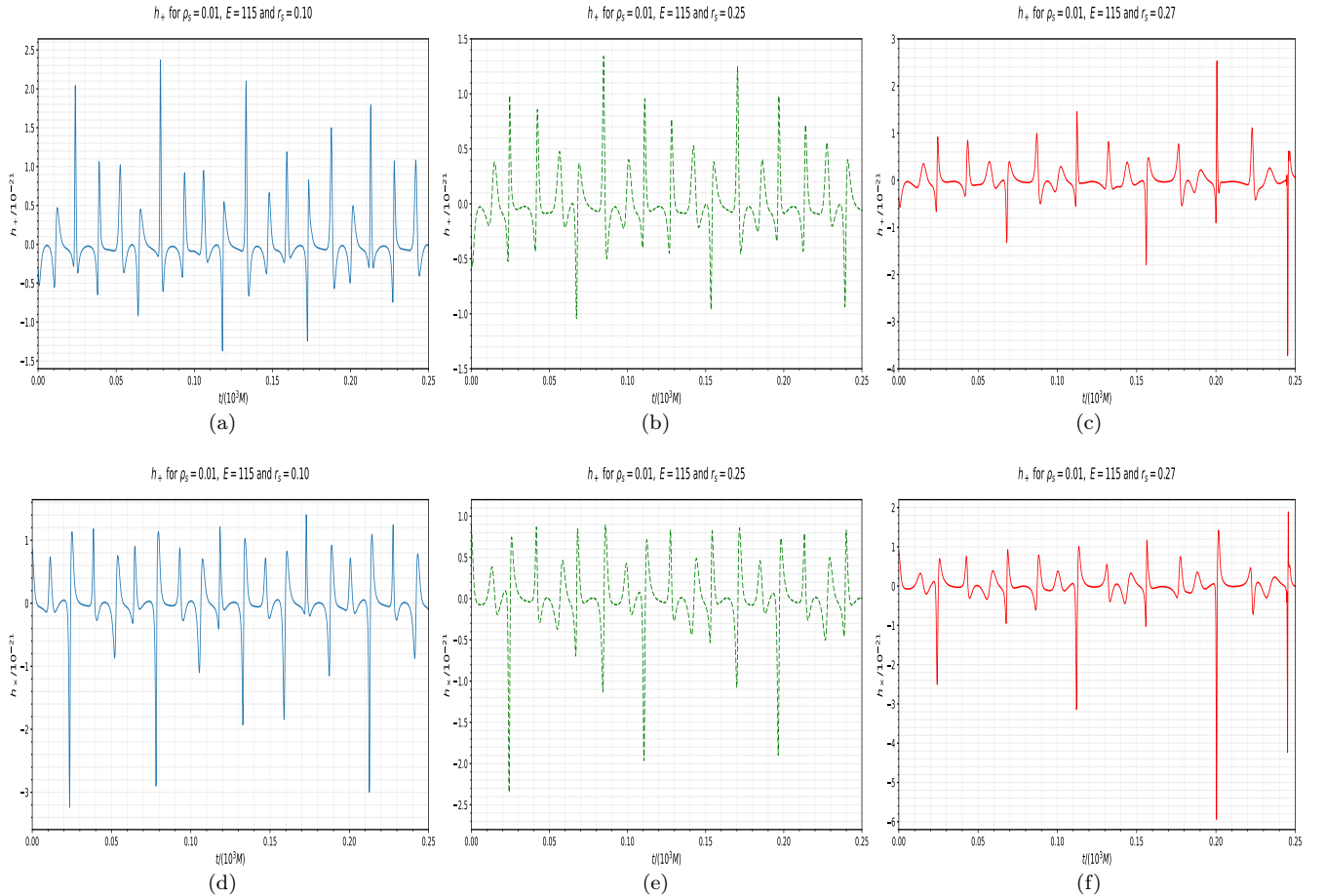


FIG. 3: Gravitational waveforms of the  $+$  and  $\times$  modes corresponding to the non-chaotic, onset-of-chaos and chaotic orbits for fixed  $\rho_s = 0.01$ ,  $E = 115$  with variations in DM halo's scale radius  $r_s$  as our considered Case-IV. Here the time range is shown from 0 to 0.25 in unit of  $t/(10^3 M)$ .

In Fig. 4, we represent the averaged GWs amplitude across all directions and the energy emission rate of the associated GWs corresponding to non-chaotic, onset-of-chaos and chaotic orbits for all of our four different cases, as mentioned in Table I. As evident from the given expressions in Eqs. (29), (30), the GWs amplitude increases when the system's mass quadrupole distribution undergoes rapid changes. Thus, it can be inferred that the averaged GWs amplitude across all directions from a chaotic orbit would likely exceed those from a non-chaotic or onset-of-chaos orbits. This has been shown in [25] for a secondary particle with spin orbiting around

a Schwarzschild BH. On the other hand, it is anticipated that the chaotic motion will also amplify the energy emission rate as well, since the energy emission rate is strongly correlated with the temporal changes in the system's mass quadrupole distribution. In this analysis, it is worth to mention that the energy emission rate for a particle moving within the Hénon-Heiles potential is studied in Ref. [92]. On the other hand in Ref. [31], Cornish *et al.* investigated the trajectory of a spinless particle in the Majumdar-Papapetrou spacetime containing two black holes and their imprints of gravitational amplitude on several orbits. From these analysis, a comparison of

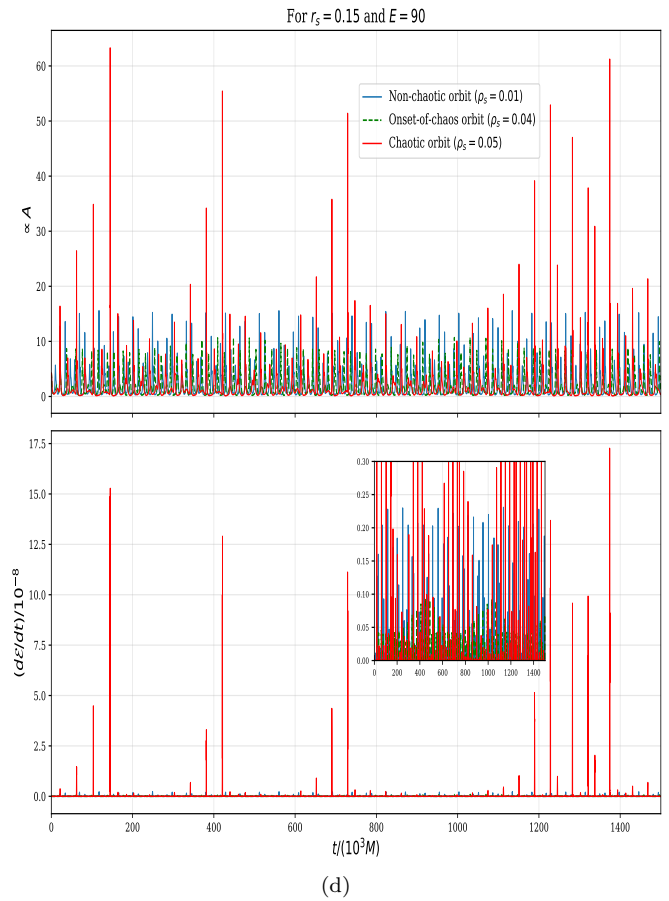
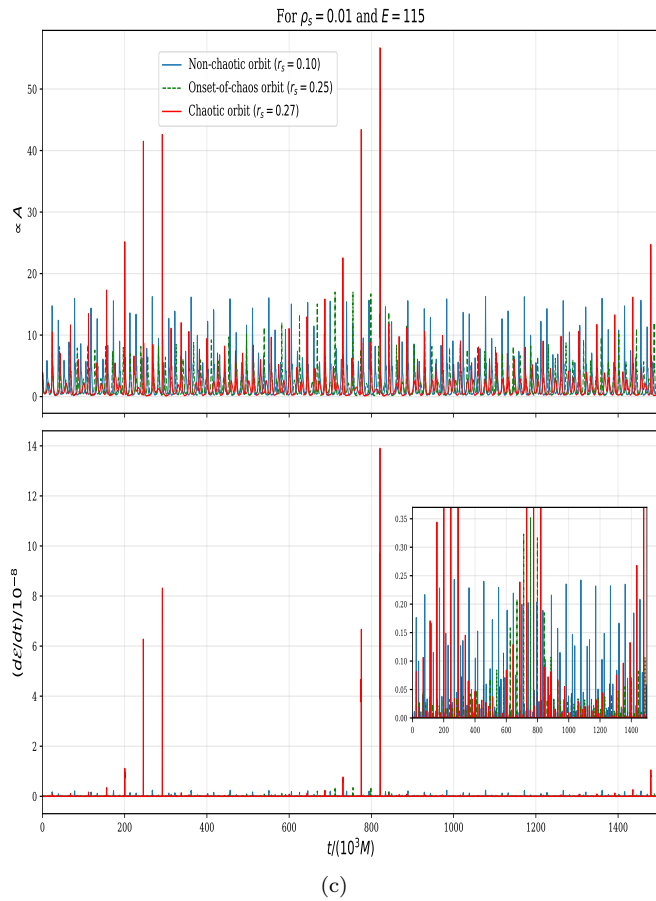
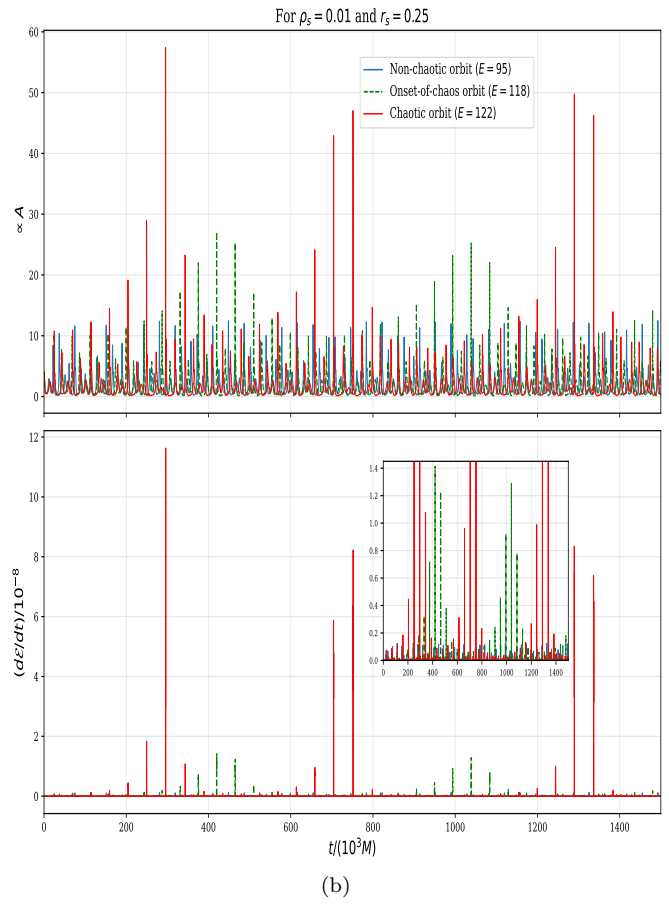
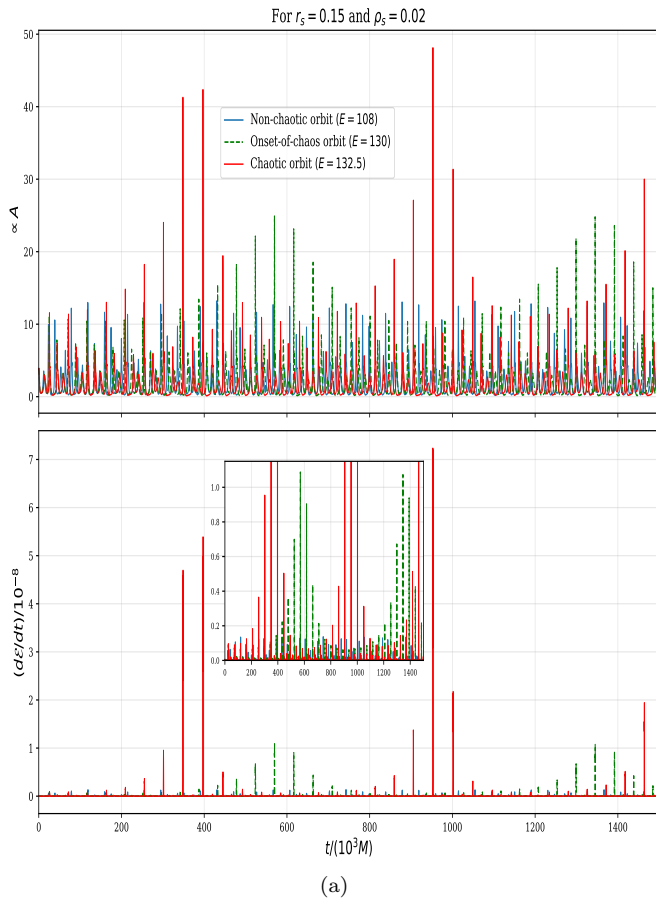


FIG. 4: The averaged GWs amplitude across all directions and the energy emission rate of the GWs corresponding to the non-chaotic, onset-of-chaos and chaotic orbits for all of the cases, mentioned in Table I.

GWs amplitude and energy emission rate from non-chaotic and chaotic orbits revealed that the chaotic dynamics leads to an increase in both amplitude and energy emission rate, clearly consistent with our findings presented in Fig. 4.

In conclusion, this subsection demonstrates that merely examining the waveforms of different orbital trajectories (chaotic, onset-of-chaos and non-chaotic) through visual inspection is inadequate to determine whether the original orbit was non-chaotic or chaotic. While there appear to be slight distinctions among non-chaotic, onset-of-chaos, and chaotic orbits, these differences may not be easily distinguishable. Therefore, in the next subsection, we analyze the frequency and energy spectrum of the gravitational waveforms for a more precise assessment.

### B. Analysis of the spectrum of gravitational waves

To further investigate the imprints of chaos in GW emissions, we analyze the frequency spectra of the gravitational waveforms associated with different types of orbit, building upon our earlier orbital computations (for more details on the orbital dynamics and computations, see [1]). This analysis involves applying discrete Fourier transforms to the time-domain gravitational waveforms shown in Fig. 1. The resulting frequency spectra, presented in Fig. 5, display the absolute values of  $\hat{h}_+(f)$  and  $\hat{h}_\times(f)$ , representing the Fourier transforms of the plus and cross polarization modes, respectively.

Our investigation of Fig. 5 reveals a fundamental distinction: Gravitational waveforms from non-chaotic orbits exhibit discrete characteristic frequencies, whereas those from chaotic orbits display a broader range of frequencies and contain many small spikes in the entire region compared with those in the non-chaotic and onset-of-chaos cases, appearing as a quasi-continuous spectrum with finite bandwidth. This spectral behavior in the Fourier analysis indicates that the signal is not periodic/regular, rather than chaotic, which is a distinctive and peculiar characteristic of chaotic systems [93]. This is one of the most important and interesting results of our paper, which is truly consistent with two previous studies on GWs energy spectra producing from the dynamics of a spinning particle around a Schwarzschild and Kerr BH by Suzuki *et al.* [25] and Keuchi *et al.* [26], respectively. Notably, while Refs. [25, 26] studied energy spectra from a spinning secondaries in Schwarzschild and Kerr spacetime, our research focuses on a spinless test particle in Schwarzschild-like BH surrounded by a DM halo, yet both approaches consistently demonstrate dis-

tinguishable spectral features between chaotic and non-chaotic orbital dynamics.

We further compute the energy spectra of GWs associated with non-chaotic, onset-of-chaos and chaotic orbits, as these are expected to become crucial observational parameters. To study the effect of the DM halo parameters  $\rho_s, r_s$  on GWs spectrum, we consider two cases as follows. Fig. 6(a) presents the energy spectra of the gravitational waveforms corresponding to each different orbits for Case-III (fixed  $E = 90$ ,  $r_s = 0.15$  with different values of  $\rho_s$ ), while Fig. 7(a) is the same for another Case-IV (fixed  $E = 115$ ,  $\rho_s = 0.01$  with different values of  $r_s$ ). It is clearly visible from the Figs. 6(a) and 7(a) that the non-chaotic orbit exhibits numerous distinct characteristic peaks at specific characteristic frequencies. For regular orbital motion, one typically observes several fundamental frequencies along with their harmonics. These results therefore indicate the presence of regular particle motion in this case. On the other hand the observed spectrum from chaotic orbit exhibits a distinct behavior compared to the non-chaotic orbit. The signal from chaotic orbit is accompanied by a numerous small, irregular spikes, which is a distinctive hallmark of chaotic dynamics. These fluctuations cause the spectral peaks to broaden significantly compared to those observed in non-chaotic system. However, beyond a characteristic frequency value  $fM \sim 10^{-0.25}$ , the energy spectra associated with non-chaotic and onset-of-chaos orbits appear to be flat and similar to white noise, suggesting a significant stochastic contribution. This interpretation, however, is misleading on an overall view. Upon closer inspection of the frequency range above  $fM \sim 10^{-0.25}$ —particularly when examining the energy spectra of the individual orbits—the distinction between regular and chaotic dynamics becomes evident (see Fig. 6(b) for Case-III and Fig. 7(b) for Case-IV). Figs. 6(b) and 7(b) clearly show that non-chaotic orbits display multiple sharp peaks (regular) at well-defined characteristic frequencies. In contrast, chaotic orbits exhibit a greater number of irregular spikes compared to non-chaotic orbits, with these spikes often overlapping and forming a quasi-continuous spectrum. This behavior is entirely distinct from that of a non-chaotic systems.

Figs. 6(b) and 7(b) also suggest a significant changes in the GWs energy spectra beyond the frequency scale  $fM \sim 10^0$ , particularly for the chaotic regime for both of the Cases-III and IV (highlighted with red color). In chaotic systems, small perturbations lead to large deviations in trajectories, causing the system may enter in a regime where a strong non-linearity in gravity is playing, as a result an unpredictable temporal fluctuations in the orbital radial dynamics is occurring and therefore the

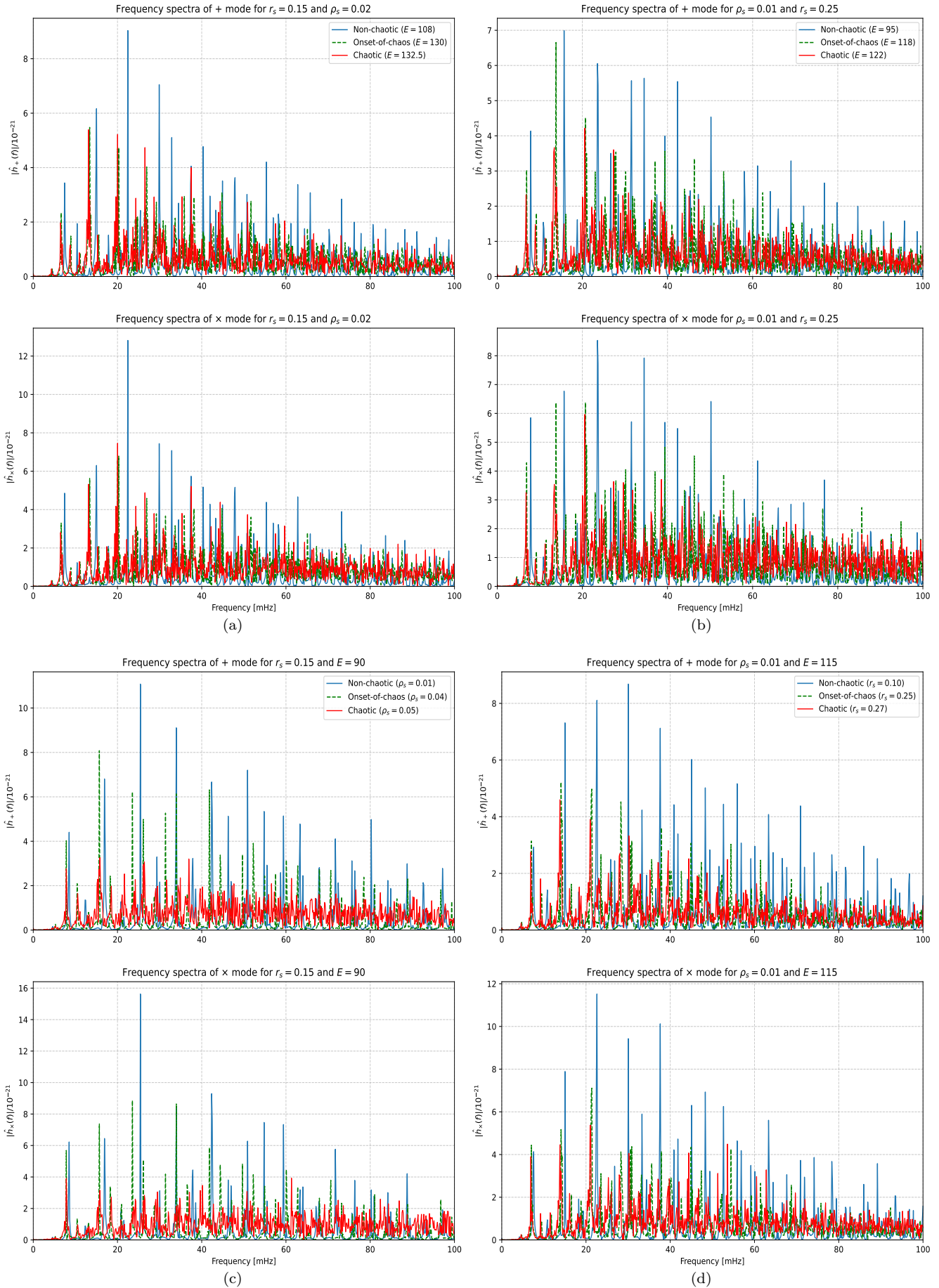




FIG. 5: Absolute values of Fourier transforms of the time-domain gravitational waveforms corresponding to the Non-chaotic, onset-of-chaos and chaotic orbits for all of the cases, mentioned in Table I.

chaotic spectrum may rise beyond this typical frequency. On the other hand, since energy is emitted in discrete, narrow frequency bands, the non-chaotic (highlighted with blue color) and onset-of-chaos (highlighted with green color) orbits show a decline in the GWs energy spectra beyond this typical frequency contrasting with the chaotic case. The spectrum likely follows an exponential or steep power-law decay, typical of ordered systems [94].

We have also examined each spectra for different orbits by magnifying its frequency range within  $fM \sim 10^0$ , which allows for a clearer interpretation of the behavior occurring just before the frequencies reach  $fM \sim 10^0$ . Figs. 6(c), 6(d), 6(e) display zoomed-in views of the energy spectra for non-chaotic, onset-of-chaos and chaotic orbits, respectively for Case-III, while Figs. 7(c), 7(d), 7(e) display the same for Case-IV, respectively. The GW energy spectra from non-chaotic orbit in Figs. 6(c) and 7(c) show many sharp peaks at certain characteristic frequencies due to its regular periodic motion, same as the case beyond  $fM \sim 10^{-0.25}$ . It is noteworthy to mention here that the appearance of such discrete characteristic frequencies from a regular or non-chaotic motions has been analytically derived by Drasco *et al.* for rotating BHs in Ref. [95], which is in well agreement with our findings. In contrast to the relatively clean (discrete) spectra of non-chaotic cases, the spectra of chaotic cases (Figs. 6(e) and 7(e)) display numerous irregular spikes. However, the peaks are not distinctly sharp; instead, they appear broadened due to the presence of numerous overlapping spikes, same as beyond  $fM \sim 10^{-0.25}$ . Such noisy spectral features are characteristic signatures of GWs emanating from chaotic orbital dynamics in EMRIs [96]. Therefore we may conclude here that the distinct spectral signatures between non-chaotic and chaotic motion for the entire frequency range  $fM \sim (10^{-3.0} - 10^{0.5})$  provide a potential tool for constraining particle motion as well as DM halo parameters.

Additionally, let us mention that that in our studies the characteristic frequencies of GWs produced by EMRIs for three different non-chaotic, onset-of-chaos and chaotic orbits fall within the detectable range. These frequencies are particularly well-suited for detection by the future space-based GWs observatories, which we will discuss in the following subsection. Although spectral analysis provides a clear distinction between regular and chaotic dynamical systems and its imprints on GWs, it would be advantageous to validate our findings using a more sophisticated approach. Such a method should be capable of distinctly characterizing chaotic and regular dynamics and its signatures in GWs. In what follows, before proceeding with further discussions on detection, let

us briefly examine the signatures of chaos in Gws through orbital and waveform recurrence analysis, inspired by the recent works of Zelenka *et al.* [97, 98].

#### IV. RECURRENCE ANALYSIS AND PHASE SPACE RECONSTRUCTION

Recurrence analysis is a powerful tool for investigating the dynamical properties of nonlinear systems from time series data. The core idea involves reconstructing the system's phase space and analyzing the recurrences of its states, which are visualized through a Recurrence Plot (RP). It serves as a tool for examining the dynamics of both regular and chaotic systems. This technique enables the estimation of dynamical invariants, including the second-order Rényi entropy and correlation dimension, while also revealing features such as unstable periodic orbits and chaotic orbits. Additionally, it provides a means to differentiate between linear and nonlinear dynamical behaviors. For comprehensive details on recurrence analysis and various metrics used to quantify recurrence plots for thorough time series examination, refer to the following Refs. [99, 100]. Below, we give a brief discussion on the theoretical foundations and then study the computational implementation of this approach in our context.

##### A. Phase Space Reconstruction via Taken's Theorem

The phase space of a dynamical system is reconstructed from a time series  $\mathbf{X}_i$  of dimension  $n$  and length  $l \geq i \in \mathbb{N}$  using the time-delay embedding method proposed by Takens [101]. According to Taken's theorem, the reconstructed time series is defined as

$$\mathbf{Y}_i = (\mathbf{X}_i, \mathbf{X}_{i+\tau}, \dots, \mathbf{X}_{i+\tau(d-1)}) ,$$

where  $\tau \in \mathbb{N}$  is the time delay and  $d \in \mathbb{N}$  is the embedding dimension, which are two free parameters. Here the reconstructed time series has a dimension of  $(n.d)$  and also has reduced length  $l - \tau(d - 1) = L \geq i \in \mathbb{N}$ . The trivial case  $d = 1$  corresponds to no reconstruction. The theorem guarantees that for sufficiently large  $d$  and suitable  $\tau$ , the reconstructed attractor is topologically equivalent to the original system's attractor.

It is worthy to mention that this method establishes a diffeomorphism between the original and reconstructed phase spaces under certain conditions [101].

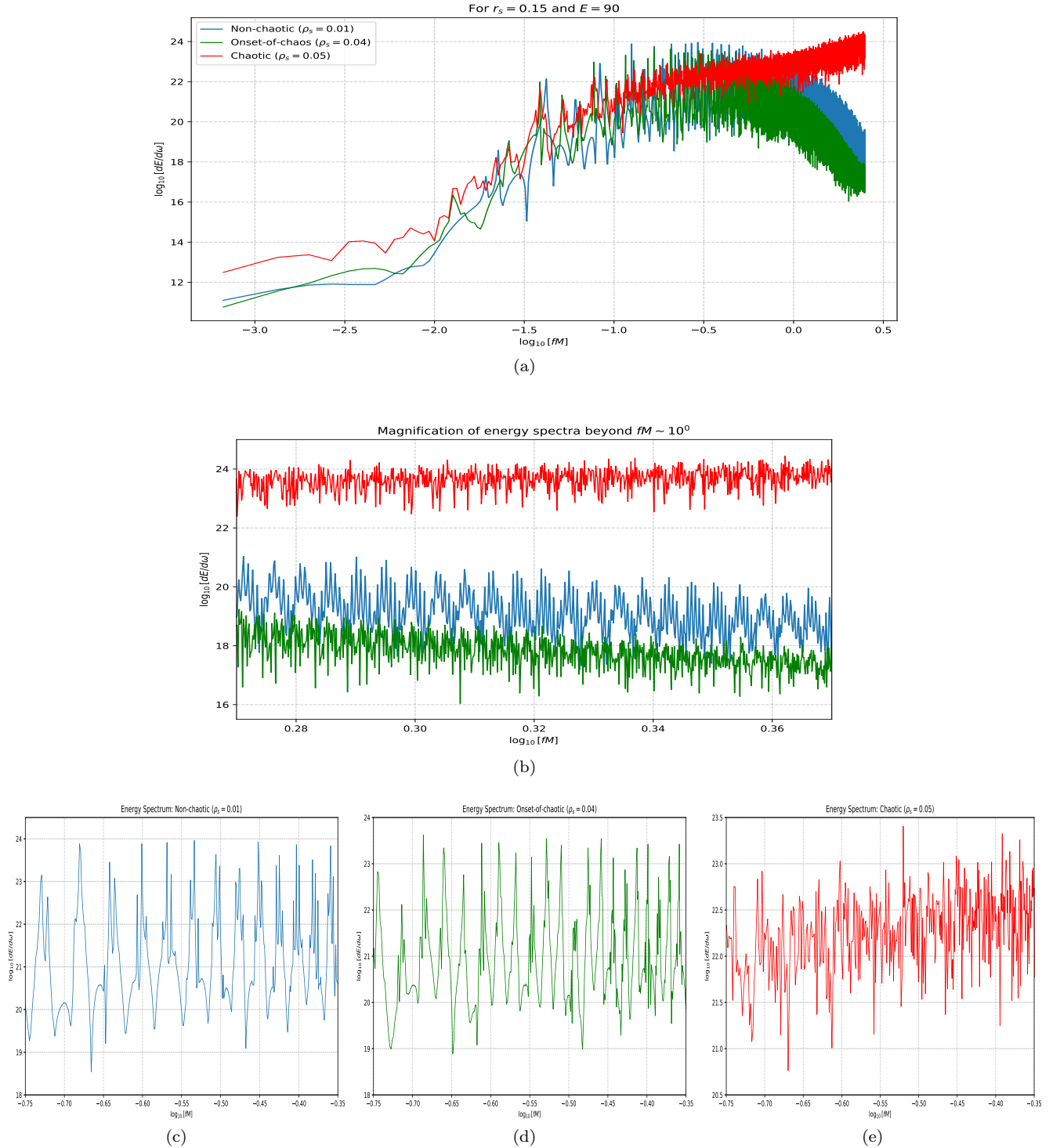


FIG. 6: Fig. 6(a) presents the GWs energy spectra corresponding to different orbits for Case-III (fixed  $r_s = 0.15$ ,  $E = 90$  with various  $\rho_s$ ). For frequencies  $fM \geq 10^0$ , both the non-chaotic and onset of chaos orbits exhibit a decay in their respective energy spectra. But this decay feature is notably absent in the case of chaotic orbit.

However, the zoomed-in view beyond  $fM \sim 10^{-0.25}$  is represented in Fig. 6(b), where the blue curve corresponds to a non-chaotic orbit ( $\rho_s = 0.01$ ), the green curve indicates the onset of chaos ( $\rho_s = 0.04$ ), and the red curve represents a fully chaotic orbit ( $\rho_s = 0.05$ ).

Figs. 6(c), 6(d), and 6(e) display magnified views of the energy spectra for non-chaotic, onset-of-chaos, and chaotic orbits within the frequency  $fM \sim 10^0$ , respectively. Fig. 6(c) reveals numerous sharp peaks at specific characteristic frequencies, a signature of regular motion, same as in Fig. 6(b). In contrast, Fig. 6(e) shows broader peaks with additional overlapping spikes, a consequence of the chaotic nature of the orbit, same as in Fig. 6(b).

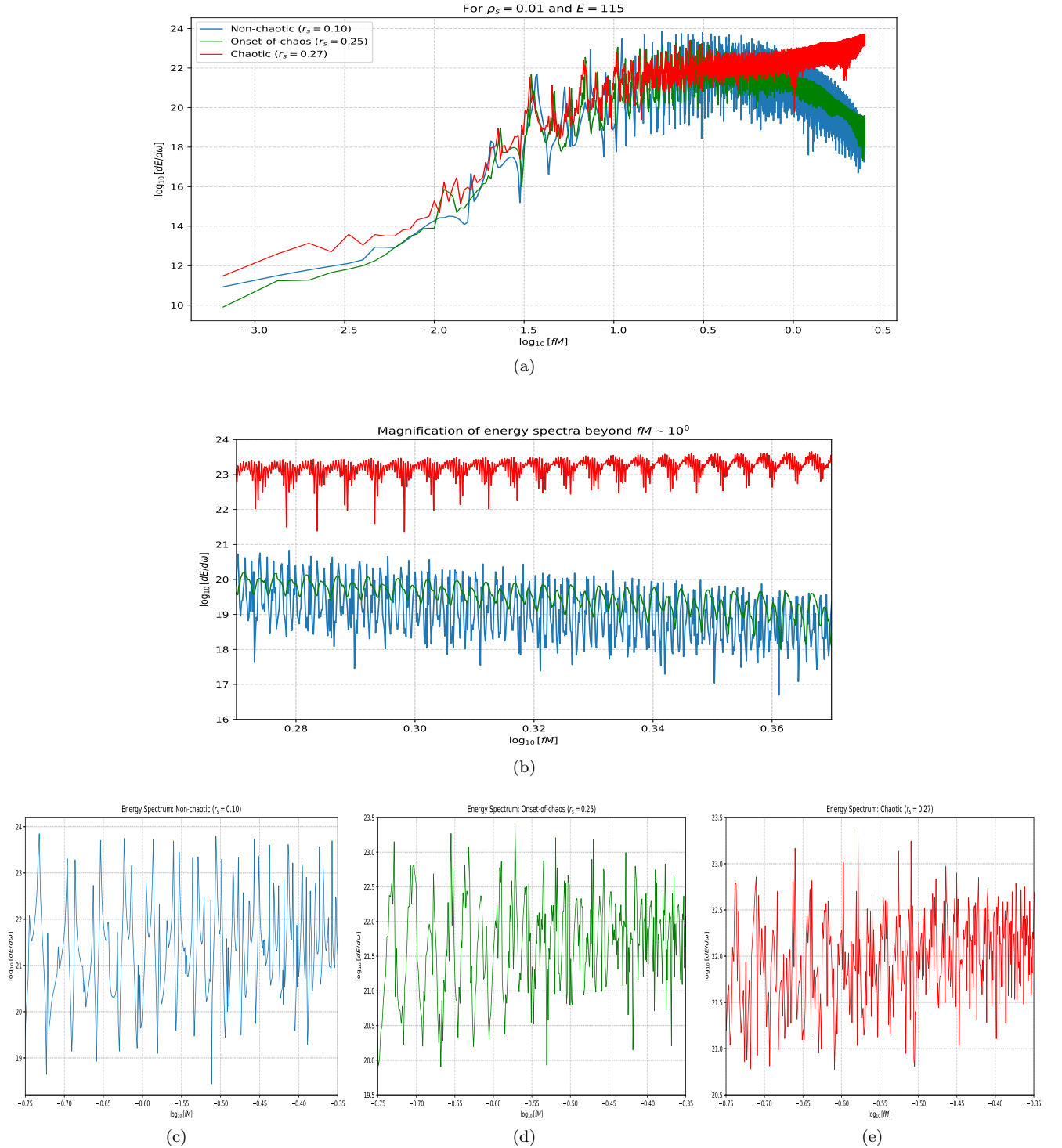


FIG. 7: Fig. 7(a) presents the GWs energy spectra corresponding to different orbits for Case-IV (fixed  $\rho_s = 0.01$ ,  $E = 115$  with various  $r_s$ ). For frequencies  $fM \geq 10^0$ , both the non-chaotic and onset of chaos orbits exhibit a decay in their respective energy spectra. But this decay feature is notably absent in the case of chaotic orbit.

However, the zoomed-in view beyond  $fM \sim 10^{-0.25}$  is represented in Fig. 7(b), where the blue curve corresponds to a non-chaotic orbit ( $r_s = 0.10$ ), the green curve indicates the onset of chaos ( $r_s = 0.25$ ), and the red curve represents a chaotic orbit ( $r_s = 0.27$ ).

Figs. 7(c), 7(d), and 7(e) display magnified views of the energy spectra for non-chaotic, onset-of-chaos, and chaotic orbits within the frequency  $fM \sim 10^0$ , respectively. Fig. 7(c) reveals numerous sharp peaks at specific characteristic frequencies, a signature of regular motion, same as in Fig. 7(b). In contrast, Fig. 7(e) shows broader peaks with additional overlapping spikes, a consequence of the chaotic nature of the orbit, same as in Fig. 7(b).

- Selection of time delay ( $\tau$ ): The time delay  $\tau$  is generally chosen as the first local minimum of the mutual information (MI) between the time series and its delayed version. The MI for a delay  $\tau$  is computed by the following definition.

$$I(\tau) = \sum_{i,j} p_{i,j}(\tau) \log \frac{p_{i,j}(\tau)}{p_i p_j}$$

where  $p_{i,j}(\tau)$  is the joint probability of observing  $\mathbf{X}_i$  in bin  $i$  and  $\mathbf{X}_{i+\tau}$  in bin  $j$ .  $p_i, p_j$  are marginal probabilities. The first minimum of  $I(\tau)$  indicates the delay where the time series provides maximal independent information.

- Selection of embedding dimension ( $d$ ): The embedding dimension  $d$  is determined using the False Nearest Neighbors (FNN) algorithm [102]. A false nearest neighbor is a point that appears close in dimension  $d$  but becomes distant when embedded in  $d + 1$  dimensions, indicating insufficient unfolding of the attractor. A neighbor is considered false if the following condition holds:

$$\frac{\|\mathbf{X}_i^{(d+1)} - \mathbf{X}_j^{(d+1)}\|}{\|\mathbf{X}_i^{(d)} - \mathbf{X}_j^{(d)}\|} > f$$

The smallest  $d$  where the fraction of FNN drops below a threshold (e.g., 5% in our analysis) is selected as the optimal embedding dimension. Ofcourse an optimal  $d$  minimizes the fraction of FNNs (ideally reducing it to zero).

## B. Recurrence Plot Construction

A Recurrence Plot (RP) visualizes the recurrences of states in the reconstructed phase space. The RP matrix  $\mathcal{R}$  is defined as the following [99, 100].

$$\mathcal{R}_{ij} = \begin{cases} \Theta(\varepsilon - \|\mathbf{X}_i - \mathbf{X}_j\|) & i \neq j \\ 0 & i = j \end{cases},$$

where  $\Theta$  is the Heaviside function and  $\varepsilon$  is known as the recurrence threshold. The free parameter  $\varepsilon$  is chosen adaptively to achieve a fixed Recurrence Rate (RR), defined as the fraction of recurrent points in the RP as the following.

$$\mathcal{RR} = \frac{1}{l^2} \sum_{i,j=1}^N \mathcal{R}_{ij}. \quad (31)$$

By construction, the recurrence matrix is symmetric. Therefore,  $\mathcal{R}_{ij} = 1$  indicates a recurrence at times  $i$  and  $j$ , meaning  $\mathbf{X}_i$  and  $\mathbf{X}_j$  lie within a specified small threshold distance.

Visualizing this matrix as a graph with axes  $i$  and  $j$  representing times  $t_i$  and  $t_j$ , where a dot marks the nonzero entries, yields a Recurrence Plot (RP).

RPs can be visually inspected to identify fundamental dynamical features, particularly to distinguish linear from nonlinear behavior. For periodic or quasiperiodic time series, a delay  $\Delta i$  exists where recurrences appear for sufficiently large  $\varepsilon$ , satisfying  $\forall i \mathcal{R}_{i,i+\Delta i} = 1$ . This results in diagonal lines parallel to the main diagonal, offset by  $\Delta i$  either in the vertical or in the horizontal direction.

On the other hand in chaotic systems, this regular structure emerges only during chaotic (irregular) phases, where a chaotic orbit approaches a stability island and temporarily mimics regular behavior over an interval  $\mathcal{I}$ . The corresponding RP region  $\mathcal{I} \times \mathcal{I}$  exhibits diagonal-parallel lines, forming a regular-looking square along the main diagonal. If chaotic behavior occurs in intervals  $\mathcal{I}_1$  and  $\mathcal{I}_2$ , the region  $(\mathcal{I}_1 \times \mathcal{I}_2) \cup (\mathcal{I}_2 \times \mathcal{I}_1)$  may either display a similar structure if the orbit revisits the same island or remain empty if different islands are involved. This creates the characteristic square-like patterns in RPs [97, 98].

## C. Signature of chaos through recurrence analysis of orbits and gravitational waveforms

An additional benefit of recurrence analysis is its applicability to time series data, which is particularly useful when examining GW strain signals in our study. Therefore, in this work, we evaluate the effectiveness of recurrence analysis by comparing its results with those obtained from the conventional Poincaré section and Lyapunov exponent methods.

We first begin by performing recurrence analysis on the radial coordinate  $r$  along the orbit at constant time interval  $\Delta t$  by generating a time series for two of our cases i.e., for fixed  $E = 90$   $r_s = 0.15$  with different values of the central density  $\rho_s$  (Case-III) and for fixed  $E = 115$   $\rho_s = 0.01$  with different values of the scale radius  $r_s$  (Case-IV). This particular time series is used to construct the radial recurrence plots and their corresponding reconstructed phase space (showing in 3 dimensions) along each orbits. We set a fixed recurrence rate ( $\mathcal{RR}$ ) to 0.06 for non-chaotic orbit, 0.08 for onset-of-chaos orbit, whereas for chaotic orbit, a higher value of  $\mathcal{RR} = 0.15$  proves more suitable for both of the Cases-III and IV.

The recurrence threshold  $\varepsilon$  is determined by setting a fixed  $\mathcal{RR}$ . We have also utilized the Euclidean norm [99, 103] in this numerical computation. In the recurrence analysis, the time series is standardized to achieve zero mean and unit standard deviation. To reconstruct the phase space trajectory, we employ the embedding method. The embedding dimension  $d$  is computed for each time series using the FNN algorithm, while the embedding time delay  $\tau$  is identified as the first minimum of the time-delayed mutual information, as described in Subsecs. IV A and IV B.

The computed recurrence plots of orbit along radial direction are displayed in Figs. 8 and 10 for Case-III and IV, respectively. A visual examination of these plots



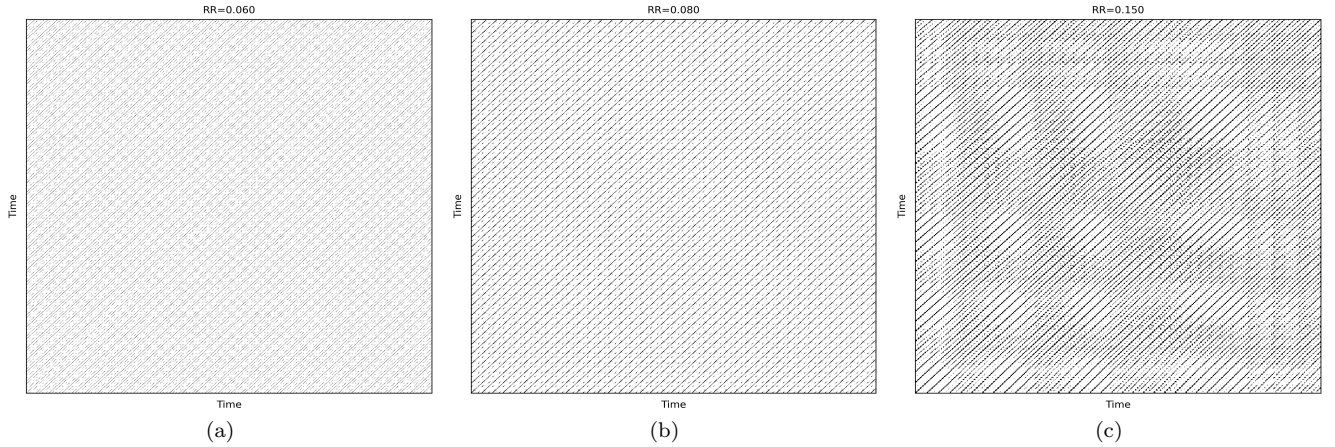


FIG. 8: Recurrence plots illustrating radial coordinate  $r$  along three distinct orbits for Case-III, with fixed parameters  $r_s = 0.15$  and  $E = 90$ , are presented. Fig. 8(a) displays the non-chaotic (regular) orbit corresponding to  $\rho_s = 0.01$ . For this non-chaotic orbit, the embedding parameters are  $d = 4$ ,  $\tau = 13$ , and  $\epsilon = 0.6209$ , with a recurrence rate  $\mathcal{RR} = 0.06$ .

Fig. 8(b) shows the orbit at the onset of chaos for  $\rho_s = 0.04$ . Here, the embedding dimension is  $d = 3$ , the delay time  $\tau = 17$ , the threshold  $\epsilon = 0.7461$ , and the recurrence rate  $\mathcal{RR} = 0.08$ .

Finally, Fig. 8(c) depicts the fully chaotic orbit for  $\rho_s = 0.05$ . The parameters for this chaotic orbit are  $d = 5$ ,  $\tau = 41$ ,  $\epsilon = 1.8515$ , and  $\mathcal{RR} = 0.15$ . We observe a distinct diagonal pattern, which is characteristic of regular or non-chaotic orbit in Fig. 8(a), slowly becoming obscured by the growing of central density  $\rho_s$  in Fig. 8(c).

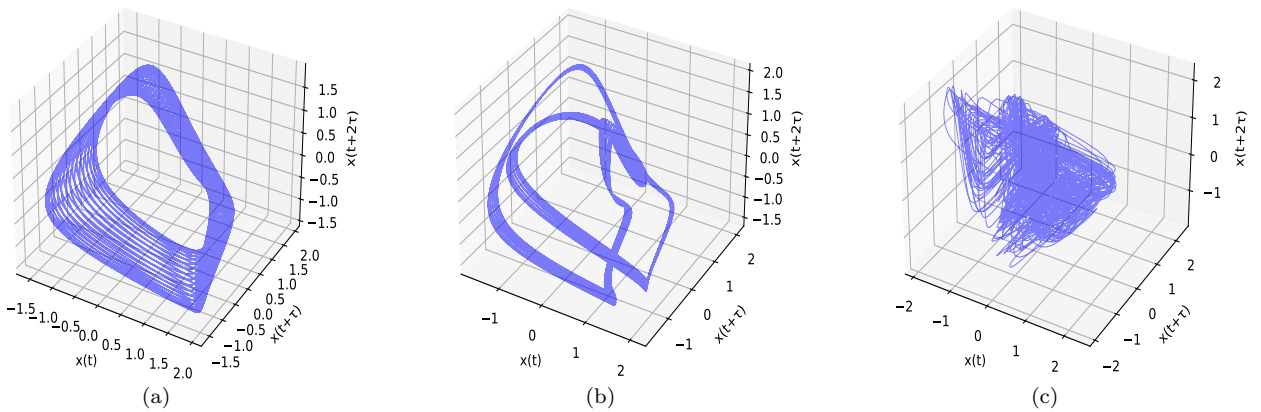


FIG. 9: The reconstructed phase space trajectories of radial coordinate  $r$  in three dimensions depict the transition from the non-chaotic to chaotic behavior for fixed parameters  $r_s = 0.15$  and  $E = 90$  in Case-III. These trajectories correspond to three distinct regimes: regular (non-chaotic), the onset of chaos, and fully developed chaotic orbits. Figures 9(c) clearly demonstrate how the system evolves from a non-chaotic state (Fig. 9(a)) to a chaotic regime, passing through an intermediate stage where chaos first begins to emerge (Fig. 9(b)).

reveal distinct patterns corresponding to non-chaotic and chaotic dynamical trajectories. In the non-chaotic case (Figs. 8(a), 10(a)), the recurrence plots exhibit a simple diagonal structure, characteristic of regular (or periodic) motion. However, this clear pattern becomes little bit

disrupted when weak chaos is introduced via the onset-of-chaos orbits (Figs. 8(b), 10(b)). Finally for  $\rho_s = 0.05$  and  $r_s = 0.25$ , we typically find a recurrence plots of strongly chaotic dynamics (Figs. 8(c), 10(c)).

The reconstructed phase space trajectories are also

shown in Figs. 9 and 11 corresponding to different orbits for both of the considered cases. It is clearly visible in Figs. 9(c), 11(c) that chaos actually appears for DM

halo parameters  $\rho_s = 0.05$  and  $r_s = 0.27$ , respectively, compared to the others (Figs. 9(a), 9(b) for Case-III and Figs. 11(a), 11(b) for Case-IV).

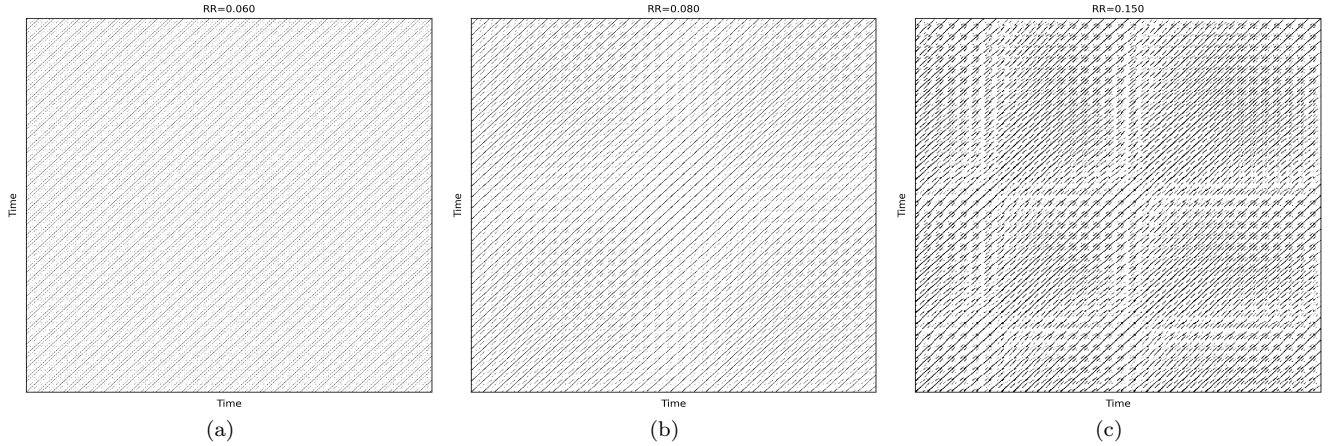


FIG. 10: Recurrence plots illustrating radial coordinate  $r$  along three distinct orbits for Case-IV, with fixed parameters  $\rho_s = 0.01$  and  $E = 115$ , are presented. Fig. 10(a) displays the non-chaotic (regular) orbit corresponding to  $r_s = 0.10$ . For this non-chaotic orbit, the embedding parameters are  $d = 4$ ,  $\tau = 34$ , and  $\epsilon = 0.6938$ , with a recurrence rate  $\mathcal{RR} = 0.06$ .

Fig. 10(b) shows the orbit at the onset of chaos for  $r_s = 0.25$ . Here, the embedding dimension is  $d = 4$ , the delay time  $\tau = 20$ , the threshold  $\epsilon = 1.0140$ , and the recurrence rate  $\mathcal{RR} = 0.08$ .

Finally, Fig. 10(c) depicts the fully chaotic orbit for  $r_s = 0.27$ . The parameters for this chaotic orbit are  $d = 4$ ,  $\tau = 23$ ,  $\epsilon = 1.5288$ , and  $\mathcal{RR} = 0.15$ . We observe a distinct diagonal pattern, which is characteristic of regular or non-chaotic orbit in Fig. 10(a), slowly becoming obscured by the growing of central density  $\rho_s$  in Fig. 10(c).

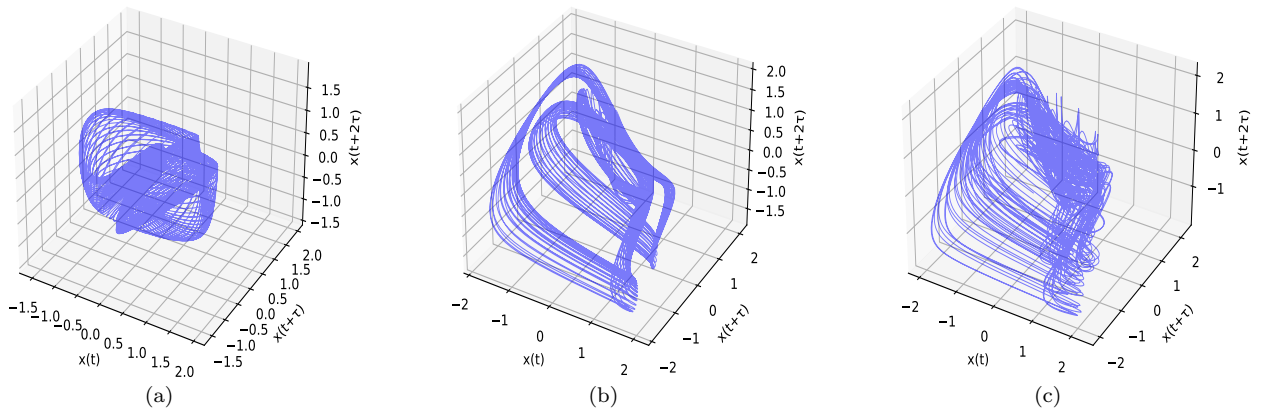


FIG. 11: The reconstructed phase space trajectories of radial coordinate  $r$  in three dimensions depict the transition from the non-chaotic to chaotic behavior for fixed parameters  $\rho_s = 0.01$  and  $E = 115$ . These trajectories correspond to three distinct regimes: regular (non-chaotic), the onset of chaos, and fully developed chaotic orbits. Figures 11(c) clearly demonstrate how the system evolves from a non-chaotic state (Fig. 11(a)) to a chaotic regime, passing through an intermediate stage where chaos first begins to emerge (Fig. 11(b)).



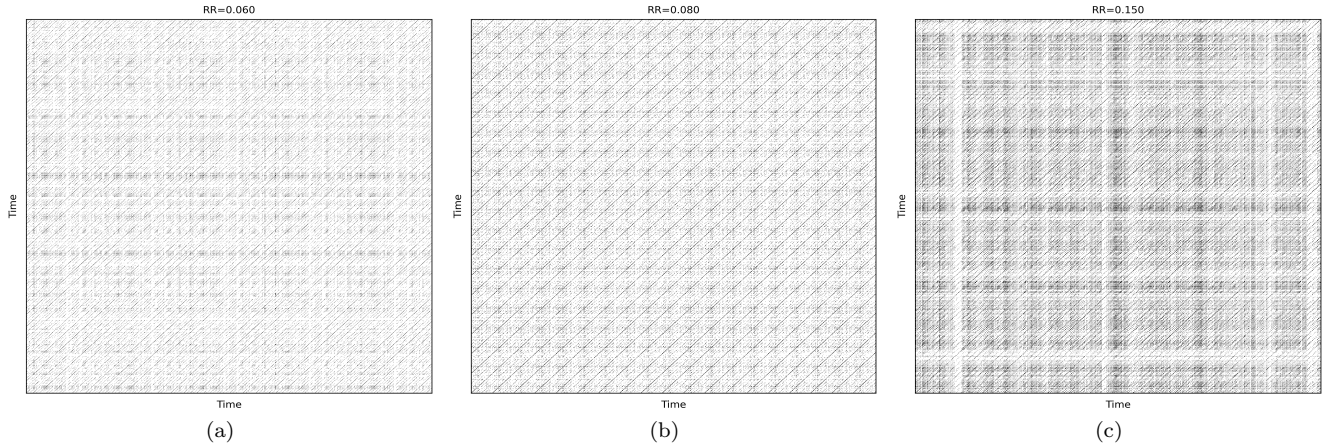


FIG. 12: Recurrence plots of the gravitational waveforms  $h_+$ , generated using the kludge scheme illustrating three distinct orbits for Case-III, with fixed parameters  $r_s = 0.15$  and  $E = 90$ , are presented. Fig. 12(a) displays  $h_+$  mode for the non-chaotic (regular) orbit corresponding to  $\rho_s = 0.01$ . For this regular motion, the embedding parameters are  $d = 8$ ,  $\tau = 14$ , and  $\epsilon = 1.7489$  with a recurrence rate  $\mathcal{RR} = 0.06$ .

Fig. 12(b) shows the  $h_+$  mode of orbit at the onset of chaos for  $\rho_s = 0.04$ . Here, the embedding dimension is  $d = 7$ , the delay time  $\tau = 16$ , the threshold  $\epsilon = 1.7835$ , and the recurrence rate  $\mathcal{RR} = 0.08$ .

Finally, Fig. 12(c) depicts the  $h_+$  waveform of fully chaotic orbit for  $\rho_s = 0.05$ . The parameters for this chaotic motion are  $d = 9$ ,  $\tau = 22$ ,  $\epsilon = 1.9769$ , and  $\mathcal{RR} = 0.15$ . We note that the plus polarization associated with non-chaotic orbits generally produces extended diagonal lines. In contrast, chaotic orbits generate a more intricate, square-shaped pattern in the corresponding plus polarization of the waveforms as the central density  $\rho_s$  increases.

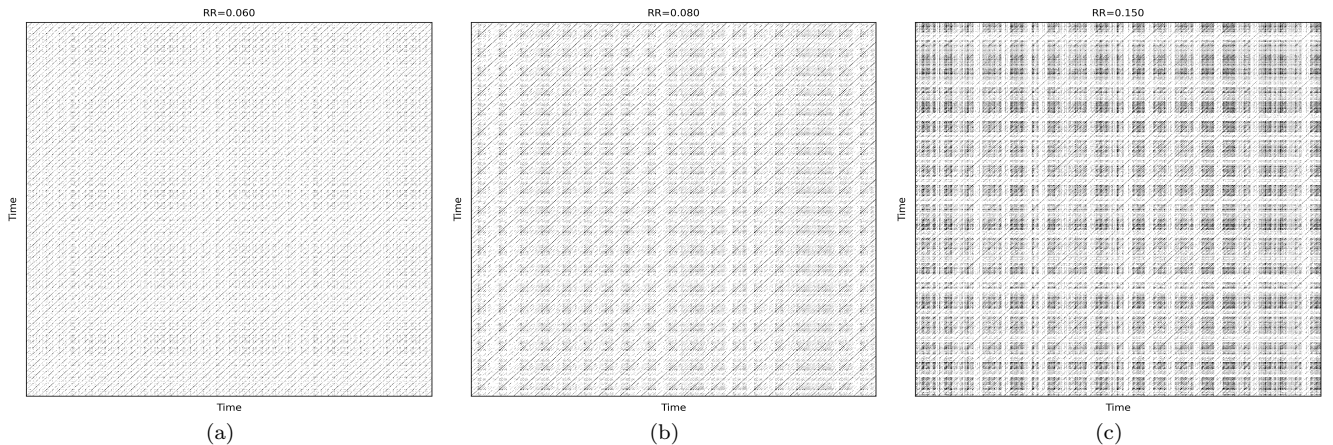


FIG. 13: Recurrence plots of the gravitational waveforms  $h_\times$ , generated using the kludge scheme illustrating three distinct orbits for Case-III, with fixed parameters  $r_s = 0.15$  and  $E = 90$ , are presented. Fig. 13(a) displays  $h_\times$  mode for the non-chaotic (regular) orbit corresponding to  $\rho_s = 0.01$ . For this regular motion, the embedding parameters are  $d = 8$ ,  $\tau = 13$ , and  $\epsilon = 1.6365$  with a recurrence rate  $\mathcal{RR} = 0.06$ .

Fig. 13(b) shows the  $h_\times$  mode of orbit at the onset of chaos for  $\rho_s = 0.04$ . Here, the embedding dimension is  $d = 7$ , the delay time  $\tau = 18$ , the threshold  $\epsilon = 1.7704$ , and the recurrence rate  $\mathcal{RR} = 0.08$ .

Finally, Fig. 13(c) depicts the  $h_\times$  waveform of fully chaotic orbit for  $\rho_s = 0.05$ . The parameters for this orbit are  $d = 10$ ,  $\tau = 16$ ,  $\epsilon = 1.6388$ , and  $\mathcal{RR} = 0.15$ . We note that similar to the plus mode, the cross polarization associated with non-chaotic orbits generally produces extended diagonal lines. In contrast, chaotic orbits generate a more intricate, square-shaped pattern in the corresponding cross polarization of the GWs as the central density  $\rho_s$  increases.



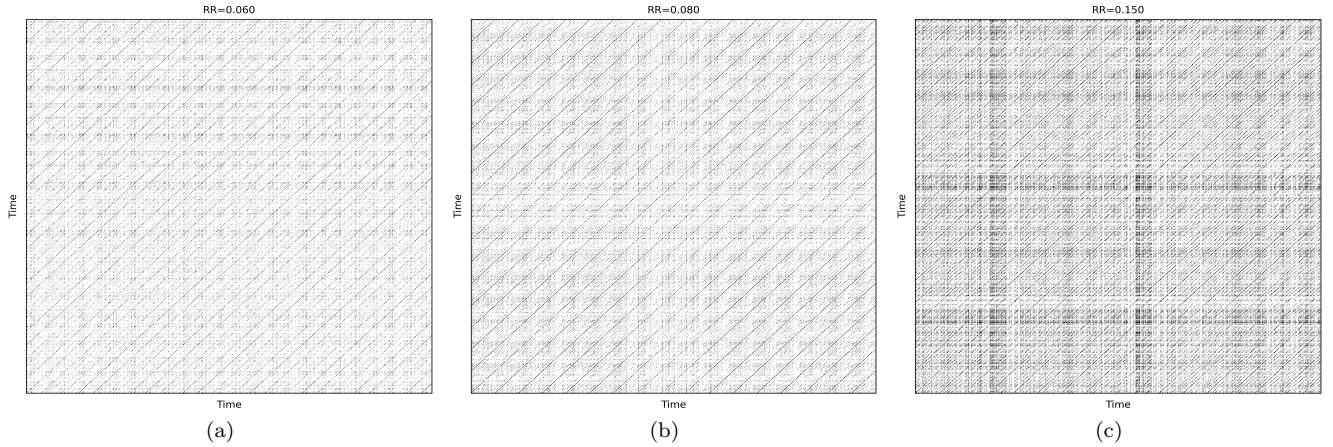


FIG. 14: Recurrence plots of the gravitational waveforms  $h_+$ , generated using the kludge scheme illustrating three distinct orbits for Case-IV, with fixed parameters  $\rho_s = 0.01$  and  $E = 115$ , are presented. Fig. 14(a) displays  $h_+$  mode for the non-chaotic (regular) orbit corresponding to  $r_s = 0.10$ . For this regular motion, the embedding parameters are  $d = 9$ ,  $\tau = 19$ , and  $\epsilon = 1.8549$  with a recurrence rate  $\mathcal{RR} = 0.06$ .

Fig. 14(b) shows the  $h_+$  mode of orbit at the onset of chaos for  $r_s = 0.25$ . Here, the embedding dimension is  $d = 9$ , the delay time  $\tau = 22$ , the threshold  $\epsilon = 2.2036$ , and the recurrence rate  $\mathcal{RR} = 0.08$ .

Finally, Fig. 14(c) depicts the  $h_+$  waveform of fully chaotic orbit for  $r_s = 0.27$ . The parameters for this chaotic motion are  $d = 9$ ,  $\tau = 15$ ,  $\epsilon = 2.4058$ , and  $\mathcal{RR} = 0.15$ . We note that the plus polarization associated with non-chaotic orbits generally produces extended diagonal lines. In contrast, chaotic orbits generate a more intricate, square-shaped pattern in the corresponding plus polarization of the waveforms as the central density  $r_s$  increases.

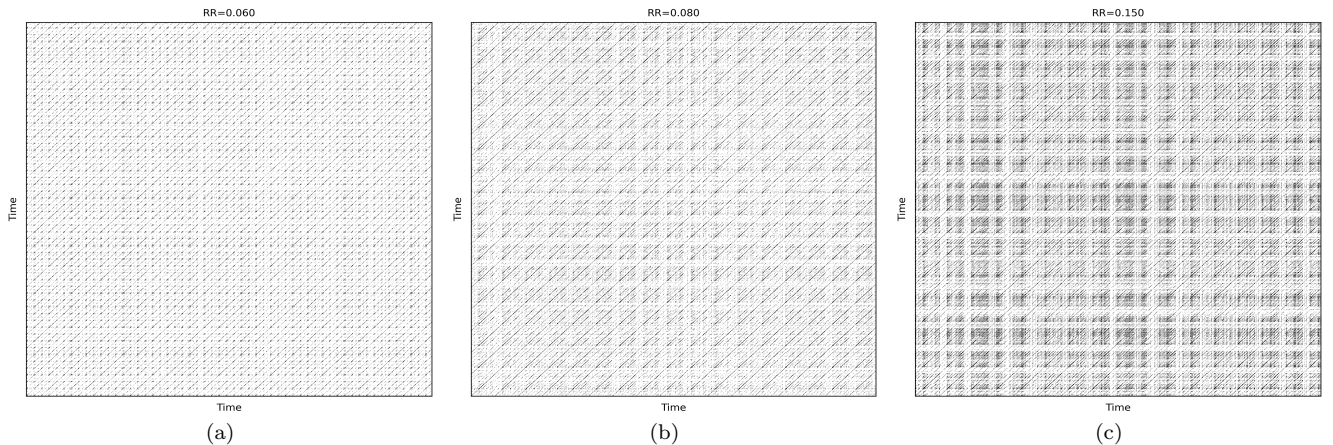


FIG. 15: Recurrence plots of the gravitational waveforms  $h_\times$ , generated using the kludge scheme illustrating three distinct orbits for Case-IV, with fixed parameters  $\rho_s = 0.01$  and  $E = 115$ , are presented. Fig. 15(a) displays  $h_\times$  mode for the non-chaotic (regular) orbit corresponding to  $r_s = 0.10$ . For this regular motion, the embedding parameters are  $d = 8$ ,  $\tau = 12$ , and  $\epsilon = 1.4702$  with a recurrence rate  $\mathcal{RR} = 0.06$ .

Fig. 15(b) shows the  $h_\times$  mode of orbit at the onset of chaos for  $r_s = 0.25$ . Here, the embedding dimension is  $d = 9$ , the delay time  $\tau = 15$ , the threshold  $\epsilon = 2.1360$ , and the recurrence rate  $\mathcal{RR} = 0.08$ .

Finally, Fig. 15(c) depicts the  $h_\times$  waveform of fully chaotic orbit for  $r_s = 0.27$ . The parameters for this orbit are  $d = 8$ ,  $\tau = 15$ ,  $\epsilon = 1.7991$ , and  $\mathcal{RR} = 0.15$ . We note that similar to the plus mode, the cross polarization associated with non-chaotic orbits generally produces extended diagonal lines. In contrast, chaotic orbits generate a more intricate, square-shaped pattern in the corresponding cross polarization of the GWs as the central density  $r_s$  increases.



Next, we apply the same recurrence analysis technique to the simulated time-domain gravitational waveforms associated with these particular orbits, namely non-chaotic, onset-of-chaos and chaotic orbits. These waveforms are numerically generated using the kludge method as outlined in Sec. III. Specifically, we analyze the time series of  $h_+$  and  $h_\times$ , as discussed in Subsec. III A. Similar to the previous analysis, we reconstruct the phase space trajectory using the delay embedding method and fix the recurrence rate to determine the threshold. The resulting recurrence plots for the two modes of gravitational waveforms are presented in Figs. 12, 13 for Case-III and Figs. 14, 15 for Case-IV. Specifically for Case-III, it is clearly visible that Figs. 12(a), 13(a) exhibit diagonal lines, a signature of ordered motion, while in Figs. 12(c), 13(c), it is characterized by square-shaped patterns, which are indicative of chaotic behavior. The similar patterns are also observed by looking the individual plots for Case-IV in Figs. 14(a), 15(a), which exhibit diagonal structure, while it is broken for the chaotic polarizations of GWs in Figs. 14(c), 15(c). Therefore these plots clearly indicate the presence of chaos and exhibit a qualitative resemblance to the recurrence plots of the corresponding orbital trajectories. Thus, we conclude that gravitational waveforms emitted by EMRIs in a galactic environment retain the signatures of chaotic dynamics, which can also be clearly identified easily through the powerful methods of recurrence analysis.

In conclusion, our analysis reveals a strong connection between the dynamical behavior of a secondary's motion around a supermassive Schwarzschild-like BH with DM halo and their corresponding gravitational waveforms. This link is evident not only in the spectrum analysis of the GWs but also in the recurrence analysis of the orbits and their associated gravitational waveforms. These findings suggest a possible realistic signature of chaos in the GWs emitted by an EMRI system in a galactic settings.

## V. SCOPES OF DETECTABILITY BY FUTURE-BASED DETECTION ANTENNAS

Our numerical analysis demonstrate that the characteristic frequencies of GWs emitted by EMRI in a supermassive Schwarzschild-like BH embedded in DM halo associated with three typical motions namely, non-chaotic, onset-of-chaos and chaotic orbits, generally fall within the observable range of space-based gravitational wave observatories, as discussed earlier in Sec. III B. This analysis allows us to evaluate the detectability of the produced GWs arising from non-chaotic, onset-of-chaos, and chaotic orbits using upcoming space-based gravitational wave detectors like LISA, TianQin, and Taiji. Prior to delving deeper into the detectability aspects of our study, for the brevity of the reader, we first provide a concise overview of the sensitivity curves for these detectors, which will be used for our analysis.

### A. LISA

The LISA sensitivity curve is derived using the formulation presented in the Ref. [104]. The effective strain spectral density characterizing the noise can be expressed as [104]

$$S_n(f) \equiv \frac{P_n(f)}{\mathcal{R}(f)} + S_c(f),$$

where  $P_n(f)$  represents the power spectral density of the detector noise and  $\mathcal{R}(f)$  denotes the instrument's signal response function averaged over sky positions and polarizations. One can approximate the LISA sensitivity curve by expanding  $P_n(f)$  and simplifying  $\mathcal{R}(f)$  in the following equation [104]:

$$S_n(f) = \frac{10}{3L^2} \left( P_{\text{OMS}}(f) + \frac{4P_{\text{acc}}(f)}{(2\pi f)^4} \right) \times \left( 1 + 0.6 \left( \frac{f}{f_*} \right)^2 \right) + S_c(f), \quad (32)$$

where  $L = 2.5 \times 10^9$  m specifies the arm length for LISA, and  $f_* = c/2\pi L \sim 19.09$  mHz defines the transfer frequency. The single-link optical metrology noise component ( $P_{\text{OMS}}(f)$ ) is given by [104]

$$P_{\text{OMS}}(f) = (1.5 \times 10^{-11} \text{ m})^2 \times \left( 1 + \left( \frac{2 \text{ mHz}}{f} \right)^4 \right) \text{ Hz}^{-1},$$

The test mass acceleration noise ( $P_{\text{acc}}(f)$ ) takes the following form [104]:

$$P_{\text{acc}}(f) = (3 \times 10^{-15} \text{ ms}^{-2})^2 \left( 1 + \left[ \frac{0.4 \text{ mHz}}{f} \right]^2 \right) \times \left( 1 + \left[ \frac{f}{8 \text{ mHz}} \right]^4 \right) \text{ Hz}^{-1},$$

Besides these instrumental noises, unresolved galactic binaries will contribute as an effective noise source, although this component is non-stationary. The galactic confusion noise ( $S_c(f)$ ) decreases over the course of the mission as more foreground sources are identified and subtracted. In our analysis, we will not consider the confusion noise and therefore following the Refs. [104], a well-designed analytical model for the sensitivity curve, which is sufficient for our purpose can be expressed as the following.

$$S_n^L(f) = \frac{10}{3L^2} \left( P_{\text{OMS}}(f) + \frac{2P_{\text{acc}}(f)}{(2\pi f)^4} \left( 1 + \cos^2 \left( \frac{f}{f_*} \right) \right) \right) \times \left( 1 + 0.6 \left( \frac{f}{f_*} \right)^2 \right), \quad (33)$$

Here it is important to note that the  $\cos^2(f/f_*)$  factor that scales the acceleration noise tends to unity in the frequency regime where acceleration noise is dominant. This simplification enables us to express the instrumental contribution to the actual sensitivity curve as presented in Eq. (32).

### B. TianQin

The TianQin sensitivity curve follows the power spectral density formulation as [18, 105]

$$S_N(f) = \frac{10}{3L^2} \left[ \frac{4S_a}{(2\pi f)^4} \left( 1 + \frac{10^{-4} \text{ Hz}}{f} \right) + S_x \right] \times \left[ 1 + 0.6 \left( \frac{f}{f_*} \right)^2 \right], \quad (34)$$

where  $L = 1.7 \times 10^8$  m represents the arm length,  $S_a = 1 \times 10^{-30} \text{ m}^2 \text{ s}^{-4} \text{ Hz}^{-1}$  quantifies the acceleration noise,  $S_x = 1 \times 10^{-24} \text{ m}^2 \text{ Hz}^{-1}$  describes the displacement measurement noise, and  $f_* = c/2\pi L \sim 280.66 \text{ mHz}$  is the transfer frequency of TianQin. Notably, Eq. 34 incorporates an additional 10/3 factor compared to the original formulation in the Ref. [18, 105], as they incorporate this factor within their waveform model rather than the power spectral density. We maintain this factor to ensure consistency with the LISA convention established by Robson *et al.* [104], enabling direct comparison between the sensitivity curves.

### C. Taiji

We consider the same form of the analytical model of sensitivity curve for Taiji as mentioned in Eq. (33). Therefore for our analysis, we proceed with the following form of the sensitivity curve for Taiji [19, 106].

$$S_n^T(f) = \frac{10}{3L^2} \left( P_{\text{dp}}(f) + \frac{2P_{\text{acc}}(f)}{(2\pi f)^4} \left( 1 + \cos^2 \left( \frac{f}{f_*} \right) \right) \right) \times \left( 1 + 0.6 \left( \frac{f}{f_*} \right)^2 \right), \quad (35)$$

where  $f_* = c/2\pi L \sim 15.90 \text{ mHz}$  is the transfer frequency and the arm length is  $L = 3 \times 10^9$  m for Taiji, a little bit longer than LISA. Here  $P_{\text{dp}}(f)$ ,  $P_{\text{acc}}(f)$  represent the power spectral density of the displacement noise and the acceleration noise, respectively, having the following forms as [19, 106]

$$P_{\text{dp}}(f) = (8.0 \times 10^{-12} \text{ m})^2 \times \left( 1 + \left( \frac{2 \text{ mHz}}{f} \right)^4 \right) \text{ Hz}^{-1},$$

$$P_{\text{acc}}(f) = (3 \times 10^{-15} \text{ ms}^{-2})^2 \left( 1 + \left[ \frac{0.4 \text{ mHz}}{f} \right]^2 \right) \times \left( 1 + \left[ \frac{f}{8 \text{ mHz}} \right]^4 \right) \text{ Hz}^{-1}.$$

It is notable to mention that both, LISA and Taiji has their same test mass acceleration noise ( $P_{\text{acc}}(f)$  and  $P_{\text{acc}}(f)$ ).

Let us now examine the detectability challenges associated with these gravitational wave detectors. To assess the detectability of GWs emitted from EMRI in a supermassive Schwarzschild-like BH embedded in a Dehnen(1, 4, 5/2)-type DM halo associated with non-chaotic, onset-of-chaos, and chaotic orbits, we calculate the characteristic strain sensitivity using the frequency spectra derived from such orbits. The characteristic strain is computed using the following definition:

$$h_c(f) = 2|f| \sqrt{|\hat{h}_+(f)|^2 + |\hat{h}_\times(f)|^2}. \quad (36)$$

Subsequently, we analyze the characteristic strain derived for three distinct orbital classifications—non-chaotic, onset-of-chaos, and chaotic—across our four different cases. These results are then contrasted with the sensitivity curves of the gravitational wave observatories, including LISA, TianQin, and Taiji. From Fig. 16, it is evident that certain portions of these strains—associated with varying central densities and radii of the DM halo, or differing energy values—above the sensitivity thresholds of LISA, TianQin, and Taiji. This suggests that upcoming space-based gravitational wave detectors could potentially observe GW signals originating from EMRIs in a supermassive Schwarzschild-like BH with DM halo associated with the regular and chaotic orbital dynamics.

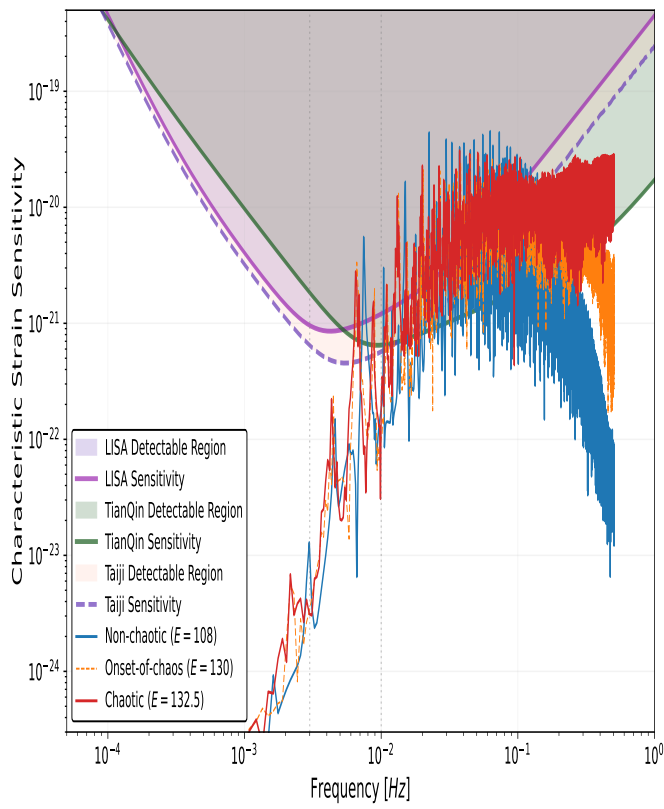
For TianQin, acceleration noise dominates at lower frequencies ( $f < 10^{-3} \text{ Hz}$ ), while laser frequency noise and shot noise become significant at higher frequencies ( $f > 10^{-1} \text{ Hz}$ ). Consequently, around  $10^{-2} \text{ Hz}$ , these noise contributions balance out, resulting in TianQin's optimal strain sensitivity [18, 105]. TianQin performs better than LISA and Taiji at frequencies above  $10^{-2} \text{ Hz}$ , due to its lower optical metrology noise. Conversely, in the lower frequency range ( $f < 10^{-3} \text{ Hz}$ ), TianQin exhibits higher noise due to its shorter arm lengths, though its acceleration noise performance remains better. Meanwhile, Taiji demonstrates slightly better sensitivity than LISA in this regime because of its marginally longer arms with respect to LISA. On the other hand, in the intermediate frequency band,  $f \sim (10^{-3} - 10^{-2}) \text{ Hz}$ , LISA and Taiji exhibit comparable sensitivity, while TianQin is less effective here due to its higher transfer frequency. The optimal frequency for GWs detector corresponds to the frequency where it achieves its best sensitivity (i.e., minimal strain noise).

In Fig. 16 for the three different orbits in all cases, we observe that TianQin can perfectly detect the chaotic dynamics arising from EMRIs in our context, whereas LISA and Taiji are only capable of detecting certain portions of it.

Additionally, it is worth noting that beyond  $f \sim 10^{-1} \text{ Hz}$ , we observe a sharp decline in the characteristic strain for non-chaotic and onset-of-chaotic motions. However, no such decline is observed for fully developed chaotic motion, due to the presence of high non-linearity.

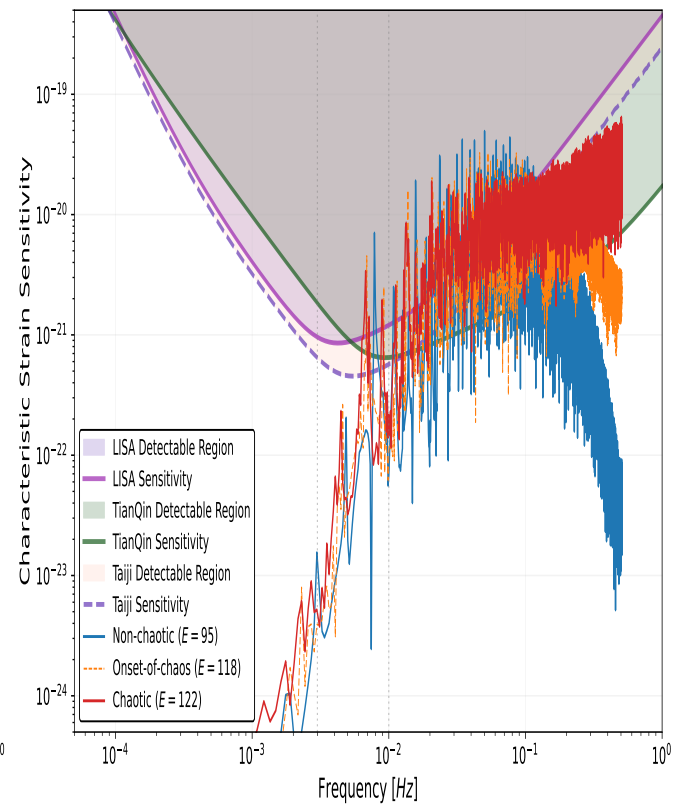
Before concluding, it is worth noting that recent studies have explored how various DM halo profiles influence the GW signals emitted by EMRIs.

Form  $r_s = 0.15$ ,  $\rho_s = 0.02$  with different values of  $E$



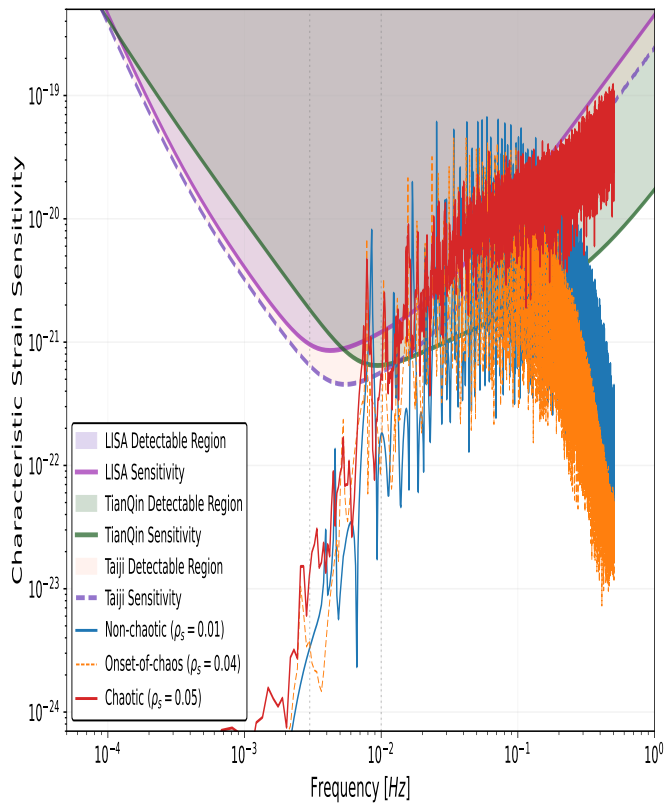
(a)

For  $\rho_s = 0.01$ ,  $r_s = 0.25$  with different values of  $E$



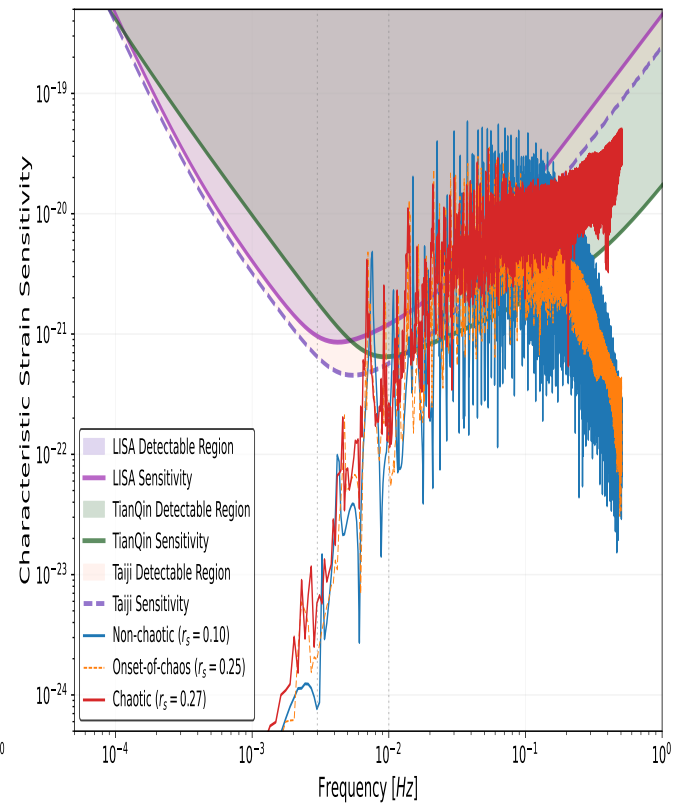
(b)

For  $r_s = 0.15$ ,  $E = 90$  with different values of  $\rho_s$



(c)

For  $\rho_s = 0.01$ ,  $E = 115$  with different values of  $r_s$



(d)

FIG. 16: Comparison of the characteristic strain  $h_c(f)$  of the gravitational waveforms generated using kludge scheme corresponding to the non-chaotic, onset-of-chaos and chaotic orbits for our four different cases with the sensitivity curves of LISA, TianQin and Taiji. In all of the figures, we plot the dimensionless characteristic strain sensitivity  $\sqrt{fS_n^L}$ ,  $\sqrt{fS_n^N}$ , and  $\sqrt{fS_n^T}$  for LISA, TianQin and Taiji, respectively.

In particular, Gliorio *et al.* investigated the distinguishability between EMRIs occurring in vacuum and those evolving around a non-rotating BH surrounded by DM profiles [107]. Based on these findings, we can infer that distinguishing vacuum EMRIs from EMRIs evolving within different DM halo configurations (such as a Dehnen(1, 4, 5/2)-type DM profile, as considered in our study)—could serve as a reliable approach for identifying GWs signature associated with both regular and chaotic orbital dynamics in EMRIs, which represent a primary observational objective for space-based detectors like LISA, TianQin, and Taiji.

## VI. DISCUSSIONS AND CONCLUSION

Let us briefly discuss and summarise our results regarding what we have achieved in this paper.

- The first part of our investigation, presented in [1], involved a detailed analysis of the chaotic dynamics exhibited by a massive test particle within an EMRI configuration. This system consists of a supermassive Schwarzschild-like BH surrounded by a Dehnen-(1, 4, 5/2) type DM halo. We began with a rigorous derivation and examination of the dynamical equations governing the motion of a massive test particle in the vicinity of the BH’s event horizon. We introduced and justified the adoption of Painlevé-Gullstrand coordinates, emphasizing their effectiveness in dealing with numerical instabilities usually encountered in the near-horizon regime. Furthermore, we discussed the strategic use of an external potentials (harmonic confinement in this case) to maintain stable particle trajectories, which is essential for investigating the chaotic transitions induced by gravitational effects in the near-horizon region.
- Subsequently, in [1], we performed an extensive numerical study of the system’s chaotic dynamics. This involved computing and analyzing Poincaré sections, tracking the orbital evolution of the EMRI, and calculating Lyapunov exponents. Our simulations demonstrated that chaotic behavior becomes markedly more pronounced with increasing particle energy and with variations in the DM halo parameters, specifically the core density  $\rho_s$  and the scale radius  $r_s$ . The emergence of chaos was clearly identified through the disintegration of regular toroidal structures in the Poincaré sections.

These qualitative observations were quantitatively validated by positive Lyapunov exponents, which were verified to be consistent with the universal chaos bounds established by the BH’s surface gravity.

- The present work is primarily dedicated to investigating the GWs emitted by an EMRI system involving a supermassive BH with a DM halo. Building upon our previous findings that the system transitions to chaos under specific parameter conditions [1], we specifically analyze the horizon’s influence during both regular (non-chaotic) and chaotic dynamical states. We observe that this behavioral transition of the system imprints itself on the GWs emitted from the near-horizon region, modifying their morphology and frequency spectrum in distinctive ways. To this end, we detailed the extraction of gravitational waveforms using the numerical kludge scheme, explicitly contrasting the signals originating from chaotic orbits with those from non-chaotic orbits. Our results demonstrate that chaotic orbits produce gravitational waveforms characterized by significantly broader and continuous frequency spectra, pronounced variations in amplitude, an enhanced energy emission rate, and distinctive recurrence patterns. These features provide a concrete and observable signature of underlying chaotic motion.
- A key novel contribution of this study is a comprehensive detectability analysis. We rigorously compared our numerically generated chaos-imprinted gravitational wave signatures with the projected sensitivity curves of upcoming space-based gravitational wave observatories, namely LISA, TianQin, and Taiji. Our findings indicate that these detectors possess the requisite sensitivity to observe and analyze GW signals emanating from chaotic EMRI systems. This analysis underscores the astrophysical feasibility and significance of detecting the imprints of chaos within gravitational wave data, forecasting substantial advancements for the field of gravitational wave astronomy.

Looking forward, our findings provide a foundation for future exploration of chaotic dynamics in other astrophysically significant BH systems. This includes rotating BHs, as well as systems affected by various DM halo profiles or other type of matter distributions. Furthermore, since our current analysis deals with a spinless secondary,



a natural extension for subsequent work would be to include the effects of secondary’s spin. In the present study, we employ the adiabatic approximation, which neglects the back-reaction of gravitational radiation on the orbital dynamics. This approach remains valid for simulations encompassing a few of orbital periods, as is the situation here. Examining the influence of gravitational radiation on the long-term behavior of chaotic orbits is a promising direction for further investigation. Additionally, our model does not account for multipole contributions beyond the quadrupole order. For the development of more precise gravitational waveform templates, it is essential to incorporate these higher-order multipole moments into the GWs expansion. Finally, with the eventual development of such accurate waveform templates, we will be positioned to study how next-generation gravitational wave detectors could potentially constrain or probe the influence of DM on chaotic orbital behavior. We look forward to addressing these challenges in subsequent studies.

### ACKNOWLEDGMENT

We are grateful to Rickmoy Samanta, Surhud More, Xian-Hui Ge, Yu-Qi Lei, Jia-Geng Jiao and Jiahang Zhong for various insightful discussions. S. Das gratefully acknowledges insightful discussions with Bala Iyer,

Prayush Kumar, Vaishak Prasad, and Alicia Sintés on chaotic dynamical system and gravitational wave during the Summer School on Gravitational-Wave Astronomy-2024 at the International Centre for Theoretical Sciences (ICTS-TIFR), Bengaluru, India and also acknowledge the support of USTC Fellowship Level A–CAS-ANSO Scholarship 2024 for PhD candidates (formerly the ANSO Scholarship for Young Talents). S. Dalui thanks the Department of Physics, Shanghai University, for providing postdoctoral funds and support from the Super Postdoctoral Fund (Grant No. 2023307) during the period of this work. BHL thanks Asia Pacific Center for Theoretical Physics, Pohang, Korea for the hospitality during his visit, where a part of this project was done. This work was supported in part by the National Key R&D Program of China (2021YFC2203100), by the National Natural Science Foundation of China (12433002, 12261131497, 125B1023), by CAS young interdisciplinary innovation team (JCTD-2022-20), by 111 Project (B23042), by CSC Innovation Talent Funds, by USTC Fellowship for International Cooperation, and by USTC Research Funds of the Double First-Class Initiative. BHL is supported by the National Research Foundation of Korea (NRF) grant RS-2020-NR049598, and Overseas Visiting Fellow Program of Shanghai University. Numerical computations were performed on the computer facilities “LINDA & JUDY” in the Particle Cosmology group (COSPA) at USTC.

- 
- [1] S. Das, S. Dalui, B.-H. Lee, and Y.-F. Cai, *Extreme-Mass-Ratio Inspirals Embedded in Dark Matter Halo I: Existence of Homoclinic Orbit and Near-Horizon Chaos*, [arXiv:2511.03657](#).
  - [2] **LIGO Scientific, Virgo** Collaboration, B. P. Abbott et al., *GW150914: The Advanced LIGO Detectors in the Era of First Discoveries*, *Phys. Rev. Lett.* **116** (2016), no. 13 131103, [[arXiv:1602.03838](#)].
  - [3] **LIGO Scientific, Virgo** Collaboration, B. P. Abbott et al., *GW170817: Observation of Gravitational Waves from a Binary Neutron Star Inspiral*, *Phys. Rev. Lett.* **119** (2017), no. 16 161101, [[arXiv:1710.05832](#)].
  - [4] **LIGO Scientific, Virgo** Collaboration, B. P. Abbott et al., *GWTC-1: A Gravitational-Wave Transient Catalog of Compact Binary Mergers Observed by LIGO and Virgo during the First and Second Observing Runs*, *Phys. Rev. X* **9** (2019), no. 3 031040, [[arXiv:1811.12907](#)].
  - [5] **LIGO Scientific, Virgo** Collaboration, R. Abbott et al., *GWTC-2: Compact Binary Coalescences Observed by LIGO and Virgo During the First Half of the Third Observing Run*, *Phys. Rev. X* **11** (2021) 021053, [[arXiv:2010.14527](#)].
  - [6] **LIGO Scientific, VIRGO** Collaboration, R. Abbott et al., *GWTC-2.1: Deep extended catalog of compact binary coalescences observed by LIGO and Virgo during the first half of the third observing run*, *Phys. Rev. D* **109** (2024), no. 2 022001, [[arXiv:2108.01045](#)].
  - [7] **LIGO Scientific, Virgo, KAGRA** Collaboration, A. G. Abac et al., *GW250114: Testing Hawking’s Area Law and the Kerr Nature of Black Holes*, *Phys. Rev. Lett.* **135** (2025), no. 11 111403, [[arXiv:2509.08054](#)].
  - [8] **KAGRA, VIRGO, LIGO Scientific** Collaboration, R. Abbott et al., *GWTC-3: Compact Binary Coalescences Observed by LIGO and Virgo during the Second Part of the Third Observing Run*, *Phys. Rev. X* **13** (2023), no. 4 041039, [[arXiv:2111.03606](#)].
  - [9] V. Korol, E. M. Rossi, P. J. Groot, G. Nelemans, S. Toonen, and A. G. A. Brown, *Prospects for detection of detached double white dwarf binaries with Gaia, LSST and LISA*, *Mon. Not. Roy. Astron. Soc.* **470** (2017), no. 2 1894–1910, [[arXiv:1703.02555](#)].
  - [10] S.-J. Huang, Y.-M. Hu, V. Korol, P.-C. Li, Z.-C. Liang, Y. Lu, H.-T. Wang, S. Yu, and J. Mei, *Science with the TianQin Observatory: Preliminary results on Galactic double white dwarf binaries*, *Phys. Rev. D* **102** (2020), no. 6 063021, [[arXiv:2005.07889](#)].
  - [11] A. Klein et al., *Science with the space-based interferometer eLISA: Supermassive black hole binaries*, *Phys. Rev. D* **93** (2016), no. 2 024003, [[arXiv:1511.05581](#)].
  - [12] H.-T. Wang et al., *Science with the TianQin observatory: Preliminary results on massive black hole binaries*, *Phys. Rev. D* **100** (2019), no. 4 043003, [[arXiv:1902.04423](#)].
  - [13] A. Sesana, *Prospects for Multiband Gravitational-Wave Astronomy after GW150914*, *Phys. Rev. Lett.* **116**

- (2016), no. 23 231102, [[arXiv:1602.06951](#)].
- [14] S. Liu, Y.-M. Hu, J.-d. Zhang, and J. Mei, *Science with the TianQin observatory: Preliminary results on stellar-mass binary black holes*, Phys. Rev. D **101** (2020), no. 10 103027, [[arXiv:2004.14242](#)].
- [15] S. Babak, J. Gair, A. Sesana, E. Barausse, C. F. Sopuerta, C. P. L. Berry, E. Berti, P. Amaro-Seoane, A. Petiteau, and A. Klein, *Science with the space-based interferometer LISA. V: Extreme mass-ratio inspirals*, Phys. Rev. D **95** (2017), no. 10 103012, [[arXiv:1703.09722](#)].
- [16] H.-M. Fan, Y.-M. Hu, E. Barausse, A. Sesana, J.-d. Zhang, X. Zhang, T.-G. Zi, and J. Mei, *Science with the TianQin observatory: Preliminary result on extreme-mass-ratio inspirals*, Phys. Rev. D **102** (2020), no. 6 063016, [[arXiv:2005.08212](#)].
- [17] LISA Collaboration, P. Amaro-Seoane et al., *Laser Interferometer Space Antenna*, [arXiv:1702.00786](#).
- [18] TianQin Collaboration, J. Mei et al., *The TianQin project: current progress on science and technology*, PTEP **2021** (2021), no. 5 05A107, [[arXiv:2008.10332](#)].
- [19] W.-R. Hu and Y.-L. Wu, *The Taiji Program in Space for gravitational wave physics and the nature of gravity*, Natl. Sci. Rev. **4** (2017), no. 5 685–686.
- [20] P. Amaro-Seoane, J. R. Gair, M. Freitag, M. Coleman Miller, I. Mandel, C. J. Cutler, and S. Babak, *Astrophysics, detection and science applications of intermediate- and extreme mass-ratio inspirals*, Class. Quant. Grav. **24** (2007) R113–R169, [[astro-ph/0703495](#)].
- [21] L. Barack and C. Cutler, *Using LISA EMRI sources to test off-Kerr deviations in the geometry of massive black holes*, Phys. Rev. D **75** (2007) 042003, [[gr-qc/0612029](#)].
- [22] N. Yunes, P. Pani, and V. Cardoso, *Gravitational Waves from Quasicircular Extreme Mass-Ratio Inspirals as Probes of Scalar-Tensor Theories*, Phys. Rev. D **85** (2012) 102003, [[arXiv:1112.3351](#)].
- [23] P. Canizares, J. R. Gair, and C. F. Sopuerta, *Testing Chern-Simons Modified Gravity with Gravitational-Wave Detections of Extreme-Mass-Ratio Binaries*, Phys. Rev. D **86** (2012) 044010, [[arXiv:1205.1253](#)].
- [24] C. J. Moore, A. J. K. Chua, and J. R. Gair, *Gravitational waves from extreme mass ratio inspirals around bumpy black holes*, Class. Quant. Grav. **34** (2017), no. 19 195009, [[arXiv:1707.00712](#)].
- [25] S. Suzuki and K.-i. Maeda, *Signature of chaos in gravitational waves from a spinning particle*, Phys. Rev. D **61** (2000) 024005, [[gr-qc/9910064](#)].
- [26] K. Kiuchi and K.-i. Maeda, *Gravitational waves from chaotic dynamical system*, Phys. Rev. D **70** (2004) 064036, [[gr-qc/0404124](#)].
- [27] L. Bombelli and E. Calzetta, *Chaos around a black hole*, Class. Quant. Grav. **9** (1992) 2573–2599.
- [28] Y. Sota, S. Suzuki, and K.-i. Maeda, *Chaos in static axisymmetric space-times. 1: Vacuum case*, Class. Quant. Grav. **13** (1996) 1241–1260, [[gr-qc/9505036](#)].
- [29] W. M. Vieira and P. S. Letelier, *Chaos around a Henon-Heiles inspired exact perturbation of a black hole*, Phys. Rev. Lett. **76** (1996) 1409–1412, [[gr-qc/9604037](#)].
- [30] S. Suzuki and K.-i. Maeda, *Chaos in Schwarzschild space-time: The motion of a spinning particle*, Phys. Rev. D **55** (1997) 4848–4859, [[gr-qc/9604020](#)].
- [31] N. J. Cornish and N. E. Frankel, *The Black hole and the pea*, Phys. Rev. D **56** (1997) 1903–1907.
- [32] A. P. S. de Moura and P. S. Letelier, *Chaos and fractals in geodesic motions around a nonrotating black hole with an external halo*, Phys. Rev. E **61** (2000) 6506–6516, [[chao-dyn/9910035](#)].
- [33] M. D. Hartl, *Dynamics of spinning test particles in Kerr space-time*, Phys. Rev. D **67** (2003) 024005, [[gr-qc/0210042](#)].
- [34] W. Han, *Chaos and dynamics of spinning particles in Kerr spacetime*, Gen. Rel. Grav. **40** (2008) 1831–1847, [[arXiv:1006.2229](#)].
- [35] M. Takahashi and H. Koyama, *Chaotic motion of Charged Particles in an Electromagnetic Field Surrounding a Rotating Black Hole*, Astrophys. J. **693** (2009) 472–485, [[arXiv:0807.0277](#)].
- [36] K. Hashimoto and N. Tanahashi, *Universality in Chaos of Particle Motion near Black Hole Horizon*, Phys. Rev. D **95** (2017), no. 2 024007, [[arXiv:1610.06070](#)].
- [37] K. Hashimoto, K. Murata, and N. Tanahashi, *Chaos of Wilson Loop from String Motion near Black Hole Horizon*, Phys. Rev. D **98** (2018), no. 8 086007, [[arXiv:1803.06756](#)].
- [38] D. Li and X. Wu, *Chaotic motion of neutral and charged particles in a magnetized Ernst-Schwarzschild spacetime*, Eur. Phys. J. Plus **134** (2019), no. 3 96, [[arXiv:1803.02119](#)].
- [39] Y.-Q. Lei, X.-H. Ge, and C. Ran, *Chaos of particle motion near a black hole with quasitopological electromagnetism*, Phys. Rev. D **104** (2021), no. 4 046020, [[arXiv:2008.01384](#)].
- [40] V. De Falco and W. Borrelli, *Detection of chaos in the general relativistic Poynting-Robertson effect: Kerr equatorial plane*, Phys. Rev. D **103** (2021), no. 6 064014, [[arXiv:2001.04979](#)].
- [41] V. De Falco and W. Borrelli, *Timescales of the chaos onset in the general relativistic Poynting-Robertson effect*, Phys. Rev. D (5, 2021) [[arXiv:2105.00965](#)].
- [42] S. Dalui, B. R. Majhi, and P. Mishra, *Presence of horizon makes particle motion chaotic*, Phys. Lett. B **788** (2019) 486–493, [[arXiv:1803.06527](#)].
- [43] S. Dalui, B. R. Majhi, and P. Mishra, *Induction of chaotic fluctuations in particle dynamics in a uniformly accelerated frame*, Int. J. Mod. Phys. A **35** (2020), no. 18 2050081, [[arXiv:1904.11760](#)].
- [44] A. Bera, S. Dalui, S. Ghosh, and E. C. Vagenas, *Quantum corrections enhance chaos: Study of particle motion near a generalized Schwarzschild black hole*, Phys. Lett. B **829** (2022) 137033, [[arXiv:2109.00330](#)].
- [45] S. Das, S. Dalui, and R. Samanta, *Near-horizon chaos beyond Einstein gravity*, Phys. Rev. D **110** (2024), no. 12 124037, [[arXiv:2405.09945](#)].
- [46] A. Deich, A. Cárdenas-Avendaño, and N. Yunes, *Chaos in quadratic gravity*, Phys. Rev. D **106** (2022), no. 2 024040, [[arXiv:2203.00524](#)].
- [47] C.-Y. Chen, F.-L. Lin, and A. Patel, *Resonant islands of effective-one-body dynamics*, Phys. Rev. D **106** (2022), no. 8 084064, [[arXiv:2206.10966](#)].
- [48] K. Destounis and K. D. Kokkotas, *Slowly-rotating compact objects: the nonintegrability of Hartle–Thorne particle geodesics*, Gen. Rel. Grav. **55** (2023), no. 11

- 123, [[arXiv:2305.18522](#)].
- [49] Z. Pan, H. Yang, L. Bernard, and B. Bonga, *Resonant dynamics of extreme mass-ratio inspirals in a perturbed Kerr spacetime*, Phys. Rev. D **108** (2023), no. 10 104026, [[arXiv:2306.06576](#)].
- [50] K. Destounis, F. Angeloni, M. Vaglio, and P. Pani, *Extreme-mass-ratio inspirals into rotating boson stars: Nonintegrability, chaos, and transient resonances*, Phys. Rev. D **108** (2023), no. 8 084062, [[arXiv:2305.05691](#)].
- [51] M. J. Rees, *Black Hole Models for Active Galactic Nuclei*, Ann. Rev. Astron. Astrophys. **22** (1984) 471–506.
- [52] J. Kormendy and D. Richstone, *Inward bound: The Search for supermassive black holes in galactic nuclei*, Ann. Rev. Astron. Astrophys. **33** (1995) 581.
- [53] G. Bertone, D. Hooper, and J. Silk, *Particle dark matter: Evidence, candidates and constraints*, Phys. Rept. **405** (2005) 279–390, [[hep-ph/0404175](#)].
- [54] J. Bovy and H.-W. Rix, *A Direct Dynamical Measurement of the Milky Way’s Disk Surface Density Profile, Disk Scale Length, and Dark Matter Profile at  $4 \text{ kpc} \lesssim R \lesssim 9 \text{ kpc}$* , Astrophys. J. **779** (2013) 115, [[arXiv:1309.0809](#)].
- [55] J. de Swart, G. Bertone, and J. van Dongen, *How Dark Matter Came to Matter*, Nature Astron. **1** (2017) 0059, [[arXiv:1703.00013](#)].
- [56] R. H. Wechsler and J. L. Tinker, *The Connection between Galaxies and their Dark Matter Halos*, Ann. Rev. Astron. Astrophys. **56** (2018) 435–487, [[arXiv:1804.03097](#)].
- [57] G. Bertone and T. Tait, M. P., *A new era in the search for dark matter*, Nature **562** (2018), no. 7725 51–56, [[arXiv:1810.01668](#)].
- [58] J. Dubinski and R. G. Carlberg, *The Structure of cold dark matter halos*, Astrophys. J. **378** (1991) 496.
- [59] A. Burkert, *The Structure of dark matter halos in dwarf galaxies*, Astrophys. J. Lett. **447** (1995) L25, [[astro-ph/9504041](#)].
- [60] J. F. Navarro, C. S. Frenk, and S. D. M. White, *The Structure of cold dark matter halos*, Astrophys. J. **462** (1996) 563–575, [[astro-ph/9508025](#)].
- [61] J. F. Navarro, C. S. Frenk, and S. D. M. White, *A Universal density profile from hierarchical clustering*, Astrophys. J. **490** (1997) 493–508, [[astro-ph/9611107](#)].
- [62] L. Hernquist, *An Analytical Model for Spherical Galaxies and Bulges*, Astrophys. J. **356** (1990) 359.
- [63] W. Jaffe, *A Simple model for the distribution of light in spherical galaxies*, Mon. Not. Roy. Astron. Soc. **202** (1983) 995–999.
- [64] S. Tremaine, D. O. Richstone, Y.-I. Byun, A. Dressler, S. M. Faber, C. Grillmair, J. Kormendy, and T. R. Lauer, *A Family of models for spherical stellar systems*, Astron. J. **107** (1994) 634, [[astro-ph/9309044](#)].
- [65] A. A. Dutton and A. V. Macciò, *Cold dark matter haloes in the Planck era: evolution of structural parameters for Einasto and NFW profiles*, Mon. Not. Roy. Astron. Soc. **441** (2014), no. 4 3359–3374, [[arXiv:1402.7073](#)].
- [66] A. W. Graham, D. Merritt, B. Moore, J. Diemand, and B. Terzić, *Empirical models for Dark Matter Halos. I. Nonparametric Construction of Density Profiles and Comparison with Parametric Models*, Astron. J. **132** (2006) 2685–2700, [[astro-ph/0509417](#)].
- [67] L. A. Urena-Lopez, T. Matos, and R. Becerril, *Inside oscillatons*, Class. Quant. Grav. **19** (2002) 6259–6277.
- [68] T. Harko, *Bose-Einstein condensation of dark matter solves the core/cusp problem*, JCAP **05** (2011) 022, [[arXiv:1105.2996](#)].
- [69] K. G. Begeman, A. H. Broeils, and R. H. Sanders, *Extended rotation curves of spiral galaxies: Dark haloes and modified dynamics*, Mon. Not. Roy. Astron. Soc. **249** (1991) 523.
- [70] V. Cardoso, K. Destounis, F. Duque, R. P. Macedo, and A. Maselli, *Black holes in galaxies: Environmental impact on gravitational-wave generation and propagation*, Phys. Rev. D **105** (2022), no. 6 L061501, [[arXiv:2109.00005](#)].
- [71] P. G. S. Fernandes and V. Cardoso, *Spinning Black Holes in Astrophysical Environments*, Phys. Rev. Lett. **135** (2025), no. 21 211403, [[arXiv:2507.04389](#)].
- [72] W. Dehnen, *A family of potential-density pairs for spherical galaxies and bulges*, Mon. Not. Roy. Astron. Soc. (11, 1993) 250–256.
- [73] B. Shukirgaliyev, A. Otebay, M. Sobolenko, M. Ishchenko, O. Borodina, T. Panamareva, S. Myrzakul, M. Kalambay, A. Naurzabayeva, E. Abdikamalov, E. Polyachenko, S. Banerjee, P. Berczik, R. Spurzem, and A. Just, *Bound mass of Dehnen models with a centrally peaked star formation efficiency*, A&A **654** (2021) A53, [[arXiv:2105.09510](#)].
- [74] R. C. Pantig and A. Övgün, *Dehnen halo effect on a black hole in an ultra-faint dwarf galaxy*, JCAP **08** (2022), no. 08 056, [[arXiv:2202.07404](#)].
- [75] M. M. Gohain, P. Phukon, and K. Bhuyan, *Thermodynamics and null geodesics of a Schwarzschild black hole surrounded by a Dehnen type dark matter halo*, Phys. Dark Univ. **46** (2024) 101683, [[arXiv:2407.02872](#)].
- [76] H. Mo, F. van de Bosch, and S. White, *Galaxy formation and evolution*. Cambridge University Press, Cambridge, United Kingdom, 2010.
- [77] A. Al-Badawi, S. Shaymatov, and Y. Sekhmani, *Schwarzschild black hole in galaxies surrounded by a dark matter halo*, JCAP **02** (2025) 014, [[arXiv:2411.01145](#)].
- [78] P. Painleve, *La mecanique classique et la theorie de relativite*, C.R. Hebd. Seances Acad. Sci. **173** (1921) 677.
- [79] S. A. Hughes, S. Drasco, E. E. Flanagan, and J. Franklin, *Gravitational radiation reaction and inspiral waveforms in the adiabatic limit*, Phys. Rev. Lett. **94** (2005) 221101, [[gr-qc/0504015](#)].
- [80] P. A. Sundararajan, G. Khanna, and S. A. Hughes, *Towards adiabatic waveforms for inspiral into Kerr black holes. I. A New model of the source for the time domain perturbation equation*, Phys. Rev. D **76** (2007) 104005, [[gr-qc/0703028](#)].
- [81] S. A. Hughes, *The Evolution of circular, nonequatorial orbits of Kerr black holes due to gravitational wave emission*, Phys. Rev. D **61** (2000), no. 8 084004, [[gr-qc/9910091](#)]. [Erratum: Phys.Rev.D 63, 049902 (2001), Erratum: Phys.Rev.D 65, 069902 (2002), Erratum: Phys.Rev.D 67, 089901 (2003), Erratum: Phys.Rev.D 78, 109902 (2008), Erratum: Phys.Rev.D

- 90, 109904 (2014)].
- [82] R. Grossman, J. Levin, and G. Perez-Giz, *Faster computation of adiabatic extreme mass-ratio inspirals using resonances*, Phys. Rev. D **88** (2013), no. 2 023002, [[arXiv:1108.1819](#)].
- [83] T. Zi and P.-C. Li, *Gravitational waves from extreme-mass-ratio inspirals in the semiclassical gravity spacetime*, Phys. Rev. D **109** (2024), no. 6 064089, [[arXiv:2311.07279](#)].
- [84] R. Ruffini and M. Sasaki, *On a Semirelativistic Treatment of the Gravitational Radiation From a Mass Thrusted Into a Black Hole*, Prog. Theor. Phys. **66** (1981) 1627–1638.
- [85] M. Sasaki, *On the Generation Mechanism of Gravitational Waves in the Vicinity of a Black Hole*, Prog. Theor. Phys. **69** (1983) 815–827.
- [86] S. Babak, H. Fang, J. R. Gair, K. Glampedakis, and S. A. Hughes, *'Kludge' gravitational waveforms for a test-body orbiting a Kerr black hole*, Phys. Rev. D **75** (2007) 024005, [[gr-qc/0607007](#)]. [Erratum: Phys.Rev.D 77, 04990 (2008)].
- [87] W. H. Press, *Gravitational Radiation from Sources Which Extend Into their Own Wave Zone*, Phys. Rev. D **15** (1977) 965–968.
- [88] K. S. Thorne, *Multipole Expansions of Gravitational Radiation*, Rev. Mod. Phys. **52** (1980) 299–339.
- [89] E. Poisson and C. Will, *Gravity: Newtonian, Post-Newtonian, Relativistic*. Cambridge University Press, 2014.
- [90] S. Yang, Y.-P. Zhang, T. Zhu, L. Zhao, and Y.-X. Liu, *Gravitational waveforms from periodic orbits around a quantum-corrected black hole*, JCAP **01** (2025) 091, [[arXiv:2407.00283](#)].
- [91] L. Landau and E. Lifshitz, *The Classical Theory of Fields*. Pergamon, Oxford, 1971.
- [92] F. Kōkubun, *Gravitational waves from the Henon-Heiles system*, Phys. Rev. D **57** (1998) 2610–2612.
- [93] A. Lichtenberg and M. Lieberman, *Regular and Chaotic Dynamics*. Springer-Verlag, New York, 1992.
- [94] H. Koyama, K. Kiuchi, and T. Konishi, *1/f fluctuations in spinning-particle motions around Schwarzschild black hole*, Phys. Rev. D **76** (2007) 064031, [[gr-qc/0702072](#)].
- [95] S. Drasco and S. A. Hughes, *Rotating black hole orbit functionals in the frequency domain*, Phys. Rev. D **69** (2004) 044015, [[astro-ph/0308479](#)].
- [96] K. Kiuchi, H. Koyama, and K.-i. Maeda, *Gravitational Wave Signals from Chaotic System: A Point Mass with A Disk*, Phys. Rev. D **76** (2007) 024018, [[arXiv:0704.0719](#)].
- [97] O. Zelenka, G. Lukes-Gerakopoulos, V. Witzany, and O. Kopáček, *Growth of resonances and chaos for a spinning test particle in the Schwarzschild background*, Phys. Rev. D **101** (2020), no. 2 024037, [[arXiv:1911.00414](#)].
- [98] O. Zelenka, O. Kopáček, and G. Lukes-Gerakopoulos, *Combining machine learning with recurrence analysis for resonance detection*, Phys. Rev. D **111** (2025), no. 8 084003, [[arXiv:2412.19683](#)].
- [99] N. Marwan, M. Carmen Romano, M. Thiel, and J. Kurths, *Recurrence plots for the analysis of complex systems*, Physics Reports **438** (2007), no. 5 237–329.
- [100] Y. Chen and H. Yang, *Multiscale recurrence analysis of long-term nonlinear and nonstationary time series*, Chaos, Solitons & Fractals **45** (2012), no. 7 978–987.
- [101] F. Takens, *Detecting strange attractors in turbulence*, in *Dynamical Systems and Turbulence*, Warwick 1980 (D. Rand and L.-S. Young, eds.), (Berlin, Heidelberg), pp. 366–381, Springer Berlin Heidelberg, 1981.
- [102] M. B. Kennel, R. Brown, and H. D. I. Abarbanel, *Determining embedding dimension for phase-space reconstruction using a geometrical construction*, Phys. Rev. A **45** (Mar, 1992) 3403–3411.
- [103] O. Kopacek, V. Karas, J. Kovar, and Z. Stuchlik, *Transition from Regular to Chaotic Circulation in Magnetized Coronae near Compact Objects*, Astrophys. J. **722** (2010) 1240–1259, [[arXiv:1008.4650](#)].
- [104] T. Robson, N. J. Cornish, and C. Liu, *The construction and use of LISA sensitivity curves*, Class. Quant. Grav. **36** (2019), no. 10 105011, [[arXiv:1803.01944](#)].
- [105] E.-K. Li et al., *Gravitational wave astronomy with TianQin*, Rept. Prog. Phys. **88** (2025), no. 5 056901, [[arXiv:2409.19665](#)].
- [106] C. Liu, W.-H. Ruan, and Z.-K. Guo, *Confusion noise from Galactic binaries for Taiji*, Phys. Rev. D **107** (2023), no. 6 064021, [[arXiv:2301.02821](#)].
- [107] S. Gliorio, E. Berti, A. Maselli, and N. Speeney, *Extreme mass ratio inspirals in dark matter halos: dynamics and distinguishability of halo models*, [arXiv:2503.16649](#).